



# Evaluation of Ceria-Added Cr<sub>3</sub>C<sub>2</sub>-25(NiCr) Coating on Three Superalloys under Simulated Incinerator Environment

Deepa Mudgal, Surendra Singh, and Satya Prakash

(Submitted March 25, 2014; in revised form October 20, 2014)

Cr<sub>3</sub>C<sub>2</sub>-25(NiCr) coating is widely used in wear, erosion and corrosion applications. In the present study, D-gun-sprayed Cr<sub>3</sub>C<sub>2</sub>-25(NiCr) coatings with and without 0.4 wt.% ceria incorporated were deposited on Superni 718, Superni 600 and Supercor 605 substrates. Hot-corrosion runs were conducted in 40 %Na<sub>2</sub>SO<sub>4</sub>-40 %K<sub>2</sub>SO<sub>4</sub>-10 %NaCl-10 %KCl environment at 900 °C for 100 cycles. Corrosion kinetics was monitored using weight gain measurements. Characterization of corrosion products was carried out by field-emission scanning electron microscopy (FESEM)/energy-dispersive spectroscopy (EDS) and x-ray diffraction (XRD) techniques. It was observed that Cr<sub>3</sub>C<sub>2</sub>-25(NiCr) coating with and without added ceria deposited on both of the Ni-based alloys showed resistance to corrosion under the given environment. Addition of ceria enhanced the adherence of the oxide to the coating during the corrosion run and reduced the overall weight gain. However, Cr<sub>3</sub>C<sub>2</sub>-25(NiCr)-coated Supercor 605 did not perform satisfactorily under this environment.

**Keywords** corrosion, D-gun, rare earth, superalloys

## 1. Introduction

Molten salt corrosion is a major cause of downtime and shutdown in the operation of waste incinerators, boilers and chemical industries, representing a large percentage of the total maintenance cost of such facilities (Ref 1). Early researchers conjectured that corrosion was caused by sulphur compounds, but it soon became evident that the dominant corrosive species are chlorides, typically in combination with alkali metals (Na, K) and heavy metals (Pb, Zn) (Ref 2). No alloy is immune to hot-corrosion attack indefinitely, although there are some alloy compositions that require a long initiation time for the hot-corrosion process to move from the initiation stage to the propagation stage (Ref 3). Hence, high-temperature coatings are generally deposited onto base materials to provide extra protection under corrosive environments. Thermal spray processes, namely plasma spray, combustion flame spray, high-velocity oxygen fuel (HVOF) spray and detonation gun spray (D-gun), offer an easy and convenient way of depositing coatings onto almost any surface (Ref 4). Among all the thermal spray processes, D-gun is one of the best methods known for producing well-adherent and low-porosity coatings (Ref 5).

Cr<sub>3</sub>C<sub>2</sub>-25(NiCr) coating is widely used for high-temperature corrosion and erosion applications, due to its high corrosion resistance along with high mechanical strength and erosion resistance properties. Its coefficient of thermal expansion is found to be compatible with superalloys generally used for high-temperature applications (Ref 6). Many studies have been done on the friction and wear behaviour of Cr<sub>3</sub>C<sub>2</sub>-NiCr coating sprayed by the D-gun process (Ref 7-12). Some studies have also reported on the oxidation and corrosion behaviour of Cr<sub>3</sub>C<sub>2</sub>-NiCr-coated steels and superalloys under isothermal and cyclic conditions (Ref 13-19).

It is well established that a small quantity of rare earth (RE) can be added to coating powder to increase the adherence between the oxide scale and coating during oxidation. It hinders the transport of species, thereby decreasing the corrosion rate (Ref 20). A number of research studies have been conducted to check the corrosion behaviour of such rare-earth-added alloys, which showed excellent results when operating in corrosive conditions. Amano et al. (Ref 21) reported the effect of adding a small amount of cerium to Ni-20Cr-5Al alloy tested under high-temperature oxidation. They observed improvement in the adhesion of the oxide scale to the substrate, which was attributed to protrusion of the surface oxide into the substrate. Kamal et al. (Ref 22) and Mahesh et al. (Ref 23-25) studied D-gun and HVOF-sprayed NiCrAl-Y + 0.4 wt.% CeO<sub>2</sub>-coated superalloys, respectively, under a Na<sub>2</sub>SO<sub>4</sub>-60 %V<sub>2</sub>O<sub>5</sub> environment at 900 °C and concluded that addition of ceria significantly improves the corrosion resistance of NiCrAlY coating. Song et al. (Ref 26) investigated the oxidation behaviour of Ni-22Cr-14W-2Mo superalloys with various La contents at 1000 and 1100 °C up to 500 h and reported an improvement in the oxidation resistance.

Deepa Mudgal, Surendra Singh, and Satya Prakash, Department of Metallurgical & Materials Engineering, Indian Institute of Technology Roorkee, Roorkee, India. Contact e-mail: deepamudgal01@gmail.com.

Very few studies have reported on the hot-corrosion behaviour of alloys and coatings under  $\text{Na}_2\text{SO}_4$ - $\text{K}_2\text{SO}_4$ - $\text{NaCl}$ - $\text{KCl}$  environments. Uusitalo et al. (Ref 27) conducted studies on low-alloy ferritic and austenitic stainless steel, five high-velocity oxygen fuel (HVOF) coatings, a laser cladding and a diffusion chromized steel under 40 wt.%  $\text{Na}_2\text{SO}_4$ , 40 wt.%  $\text{K}_2\text{SO}_4$ , 10 wt.%  $\text{NaCl}$  and 10 wt.%  $\text{KCl}$ , in both oxidizing and reducing atmospheres. They concluded that corrosion in oxidizing atmosphere in the presence of deposits was more severe than in reducing conditions. Shores et al. (Ref 28) performed corrosion tests on Fe-20 %Cr alloy under four pure salts ( $\text{Na}_2\text{SO}_4$ ,  $\text{K}_2\text{SO}_4$ ,  $\text{NaCl}$  and  $\text{KCl}$ ) and a mixture of these salts at 800 °C. They reported that alkali chlorides, unlike sulphates, support a continuous salt pathway from ambient to the metal/scale interface, allowing efficient transport of oxidant to the oxidized metal. Secondly, under oxidizing conditions, alkali chlorides have higher solubility of Fe- and Cr-containing species than do alkali sulphates. Both of these factors support higher transport rates, which according to the fluxing theory of hot corrosion will lead to faster corrosion. Ishitsuko et al. (Ref 29) studied the stability of various protective oxide films in a waste incinerator environment under  $\text{NaCl}$ - $\text{KCl}$  and  $\text{Na}_2\text{SO}_4$ - $\text{K}_2\text{SO}_4$ - $\text{NaCl}$ - $\text{KCl}$  salt mixtures with three different levels of basicity. They concluded that, in a waste incineration environment, a protective  $\text{Cr}_2\text{O}_3$  film easily dissolves in molten chlorides. There is no reported literature so far on the hot-corrosion behaviour of D-gun-sprayed  $\text{Cr}_3\text{C}_2$ - $\text{NiCr}$ +0.4 wt.%  $\text{CeO}_2$  coatings deposited on superalloys under a 40 % $\text{Na}_2\text{SO}_4$ -40 % $\text{K}_2\text{SO}_4$ -10 % $\text{NaCl}$ -10 % $\text{KCl}$  environment. In the present study, the effect of adding 0.4 wt.%  $\text{CeO}_2$  to chromium carbide nickel chromium coating sprayed onto three superalloys (Superni 718, Superni 600 and Superco 605) was observed under a 40 % $\text{Na}_2\text{SO}_4$ -40 % $\text{K}_2\text{SO}_4$ -10 % $\text{NaCl}$ -10 % $\text{KCl}$  molten salt environment at 900 °C under cyclic conditions. The environment adopted here simulates the environment of incinerators as given in the reported literature. The amount of ceria added to the coating is taken from previous reported literature where 0.4 wt.% ceria was added to  $\text{NiCrAlY}$  coating, resulting in better corrosion resistance compared with the coating without added ceria under a corrosive environment (Ref 22, 25).

## 2. Experimental

### 2.1 Development of $\text{Cr}_3\text{C}_2$ - $\text{NiCr}$ Coatings

The Ni- and Co-based superalloys (Table 1) used in the present investigation were procured from MIDHANI, Hyderabad, India in rolled and annealed condition. Specimens with dimensions of  $20 \times 15 \times 5 \text{ mm}^3$  were cut from sheet and polished using 220, 320, 400, 600 and 800 grit size emery paper followed by cloth polishing using 0.3- $\mu\text{m}$  alumina powder. Subsequently, the samples were degreased with acetone and grit blasted with alumina to roughen the surface of the specimen immediately before coating the substrate using the D-gun technique. After grit

blasting, care was taken not to touch the specimen with bare hands so as to avoid any type of contamination.

Commercially available chromium carbide nickel chromium [ $\text{Cr}_3\text{C}_2$ -25( $\text{NiCr}$ ); Praxair; Fig. 1a] coating powder was used to deposit on the substrates. The detonation gun process was used to deposit the coating powder at SVX powder M Surface Pvt. Ltd., Greater Noida, India. The optimized parameters set by the firm for coating deposition are presented in Table 2. Coating of  $\sim 200 \mu\text{m}$  was deposited onto the substrates. The thickness of the coating was achieved in four passes with 45–50  $\mu\text{m}$  coating thickness deposited per pass.

### 2.2 Development of $\text{Cr}_3\text{C}_2$ - $\text{NiCr}$ +0.4 % $\text{CeO}_2$ Powder

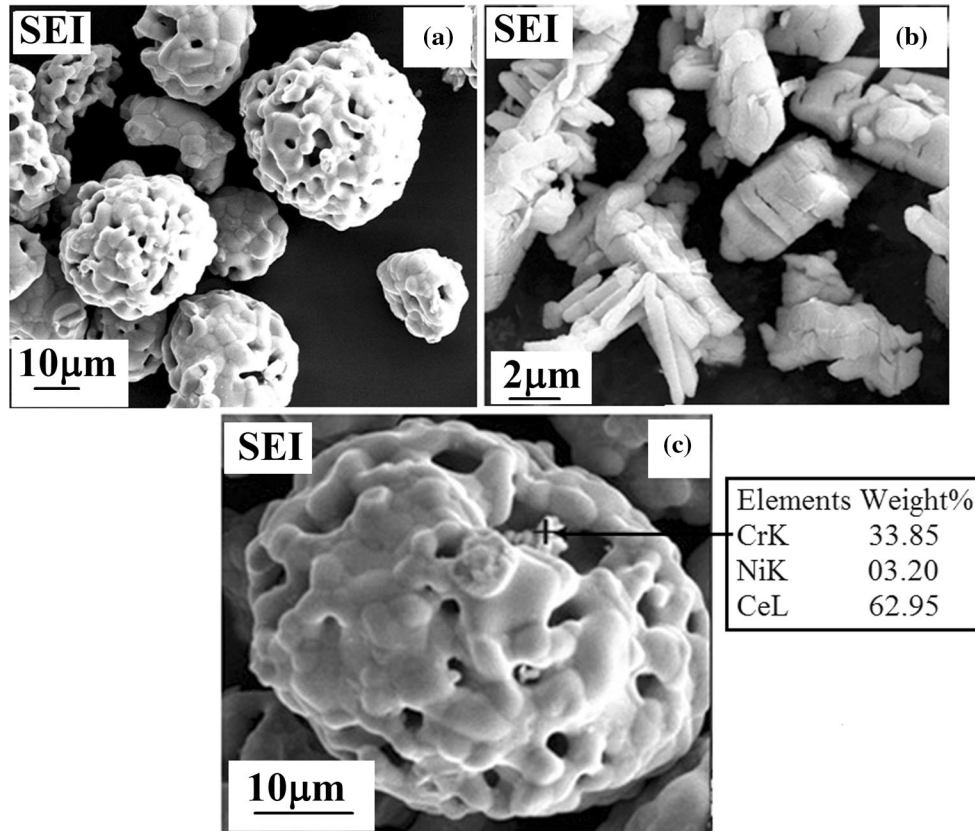
Commercially available  $\text{Cr}_3\text{C}_2$ -25( $\text{NiCr}$ ) powder (Praxair) was used, being mixed with commercially available ceria powder (Strem Chemicals).  $\text{Cr}_3\text{C}_2$ -25( $\text{NiCr}$ ) powder has a spongy-type morphology with particle size varying from 25 to 40  $\mu\text{m}$ , as shown in Fig. 1a. Ceria powder with 99.9 % purity was procured from Chempure Pvt. Ltd., having needle-like cylindrical shape and particle size less than 5  $\mu\text{m}$  (Fig. 1b). An SEM micrograph of the blended powder is shown in Fig. 1c. The amount of ceria added was adjusted to achieve 0.4 wt.% ceria in  $\text{Cr}_3\text{C}_2$ -25( $\text{NiCr}$ ) powder. The conventional jar milling method was used to mix the two powders using case-hardened steel balls at 1:1 ratio (Ref 22–25). Milling was carried out for a period of 8 h. The coating was deposited using the D-gun process with the parameters listed in Table 2. The coating was deposited on all six surfaces of the specimens.

### 2.3 Characterization Techniques

Micrographs were taken of all specimens using field-emission scanning electron microscopy (FESEM, FEI, Quanta 200F; accelerating voltage 20 kV) equipped with an Oxford X-max for EDS analysis. Secondary-electron imaging (SEI) was carried out for surface analysis, while backscattered electron imaging (BSEI) was recorded from cross-sectional surfaces. For cross-sectional analysis, coated samples were cut vertically using electrical discharge machining (EDM) wire cutting and mounted in TransOptic resin. The mounted samples were polished using 220, 320, 600 and 800 emery papers followed by alumina cloth polishing. After that, the samples were gold coated and pasted on stub. Silver paste was applied from the edge of the sample to the edge of the stub to make it conducting. For phase identification, XRD was carried out using a Bruker AXS D8 Advance diffractometer (Germany) with  $\text{Cu K}_\alpha$  radiation and a nickel filter at 30 mA under a voltage of 40 kV. The specimens were scanned at a scanning speed of 1 kcps in the  $2\theta$  range from 20° to 80°, and intensities were recorded at goniometer speed of 1°/min. The  $d$ -values corresponding to each peak along with the  $2\theta$  values are indicated on the diffractograms by the default DIFFRACplus XRD software. XRD phases were resolved using X-pert hi-score, with further confirmation from Joint Committee on Powder Diffraction Standards

**Table 1** Composition of superalloys

Name of superalloy	Elements, wt. %												
	Fe	Ni	Mn	Cr	Cu	W	Mo	Co	Si	Ti	C	Nb	Al
Superni 600	10 (max)	Bal.	0.5	15.5	...	...	...	...	0.3	...	0.021	...	...
Superco 605	3.0	10.0	1.5	20.0	...	15.0	...	Bal.	0.3	...	0.08	...	...
Superni 718	18.5	Bal.	0.18	19.0	0.15	...	3.05	...	0.18	0.9	0.04	5.13	0.5

**Fig. 1** FESEM micrographs of (a)  $\text{Cr}_3\text{C}_2\text{-NiCr}$  powder, (b)  $\text{CeO}_2$  powder and (c)  $\text{Cr}_3\text{C}_2\text{-NiCr} + 0.4\% \text{CeO}_2$  powder**Table 2** D-gun coating parameters

Parameter	$\text{Cr}_3\text{C}_2\text{-NiCr}$ coating
Oxygen/acetylene flow rate	1:1.21
Carrier gas flow rate $\text{N}_2$ , $\text{m}^3/\text{h}$	0.96
Frequency, shots/s	3
Diameter of spot (shot size), mm	20
Spraying distance from nozzle, mm	165
Powder flow rate, g/shot	1–2

**Table 3** Abbreviations for each specimen used in experiments

Coated substrate	Abbreviation
$\text{Cr}_3\text{C}_2\text{-25(NiCr)}$ -coated Superni 718	718(A)
$\text{Cr}_3\text{C}_2\text{-25(NiCr)} + 0.4\% \text{CeO}_2$ -coated Superni 718	718(B)
$\text{Cr}_3\text{C}_2\text{-25(NiCr)}$ -coated Superni 600	600(A)
$\text{Cr}_3\text{C}_2\text{-25(NiCr)} + 0.4\% \text{CeO}_2$ -coated Superni 600	600(B)
$\text{Cr}_3\text{C}_2\text{-25(NiCr)}$ -coated Superco 605	605(A)
$\text{Cr}_3\text{C}_2\text{-25(NiCr)} + 0.4\% \text{CeO}_2$ -coated Superco 605	605(B)

(JCPDS) cards if required. Coating porosity was measured from polished surface using a Zeiss Axiovert 200 MAT inverted optical microscope fitted with Axiovision multiphase release 4.1 (Germany) imaging software. Porosity values were measured by processing optical micrographs using the image analyzer in Axiovision multiphase

release 4.1 software based on American Society for Testing and Materials (ASTM) B276. A total of five images were taken for each coating at different locations, and average values are reported. The cross-sectional microhardness of the coating was measured with a load of 300 g applied for 10 s using a 402MVD (Wilson Instruments). A

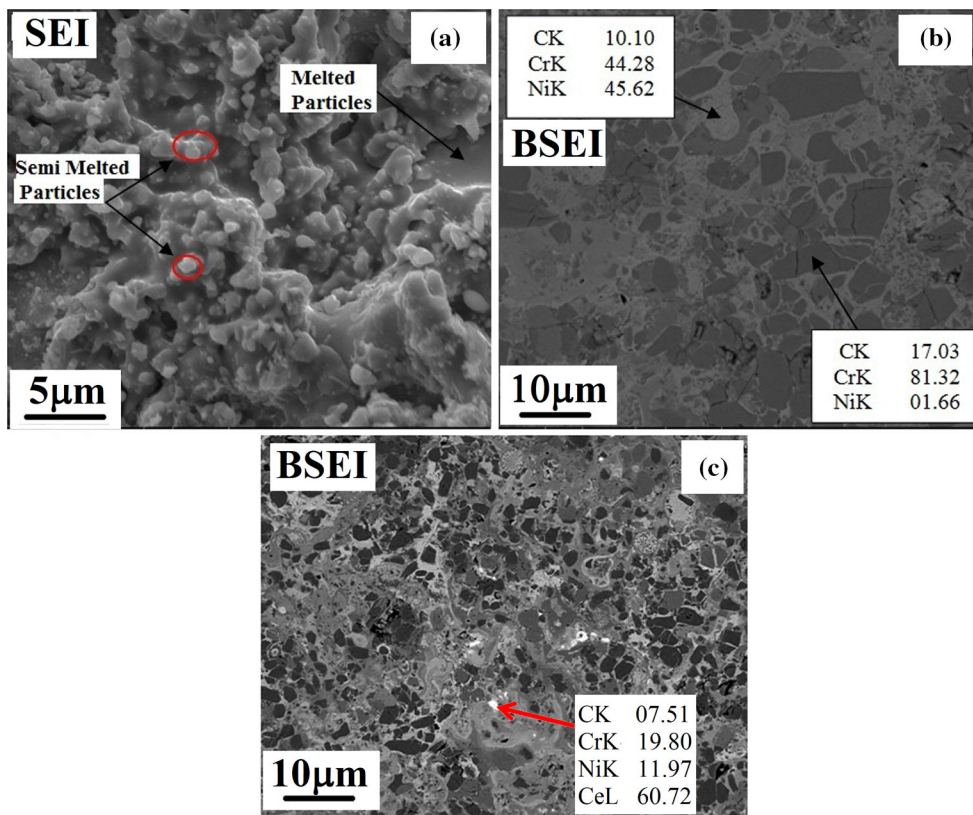


**Fig. 2** FESEM micrographs of (a) as-sprayed  $\text{Cr}_3\text{C}_2\text{-NiCr}$  coating, (b) polished  $\text{Cr}_3\text{C}_2\text{-NiCr}$  coating and (c)  $\text{Cr}_3\text{C}_2\text{-NiCr} + 0.4 \text{ wt. \% CeO}_2$  coating

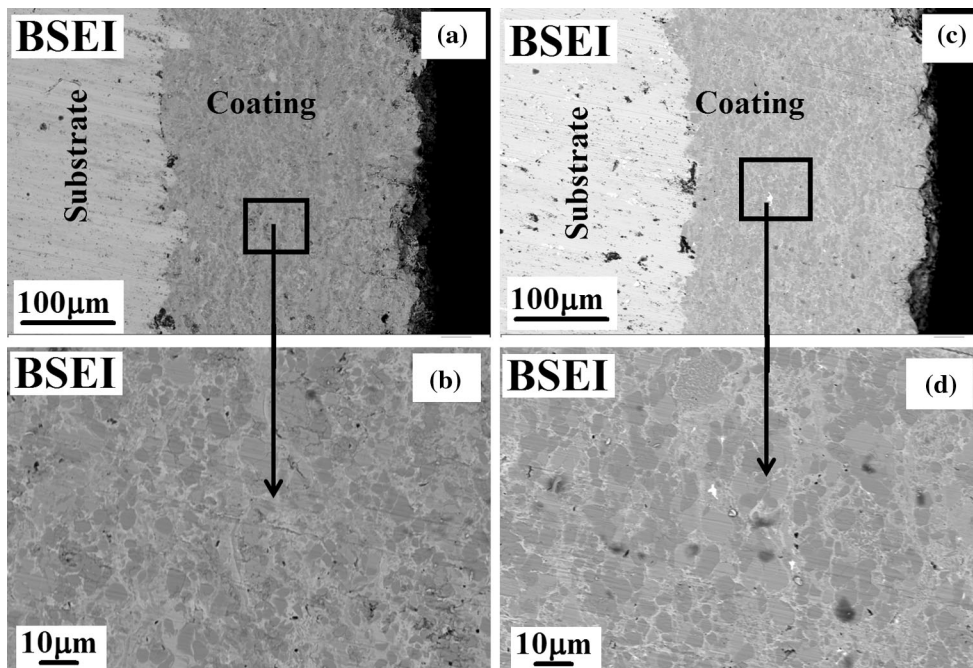


**Fig. 3** FESEM cross-sectional micrographs of unpolished  $\text{Cr}_3\text{C}_2\text{-NiCr}$  coating at (a)  $\times 500$  and (b)  $\times 5000$ , and  $\text{Cr}_3\text{C}_2\text{-NiCr} + 0.4 \text{ wt. \% CeO}_2$  coating at (c)  $\times 500$  and (d)  $\times 5000$

minimum of five readings were taken to obtain the average microhardness value.

## 2.4 Hot-Corrosion Studies

Before the hot-corrosion experiment, the dimensions of the coated samples were measured using a Sylvac digital

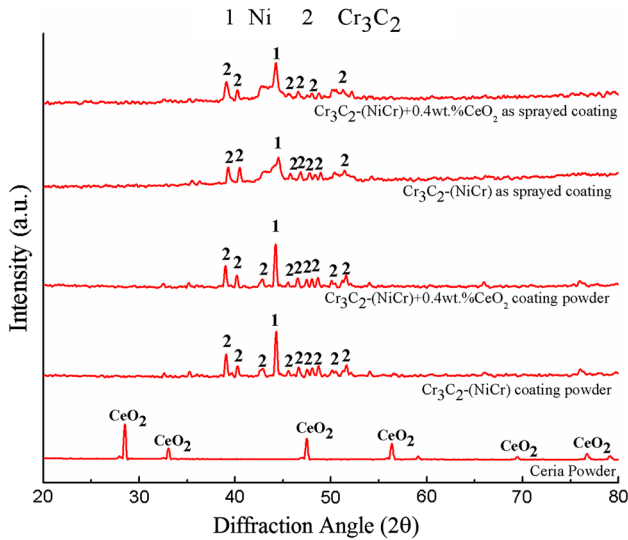
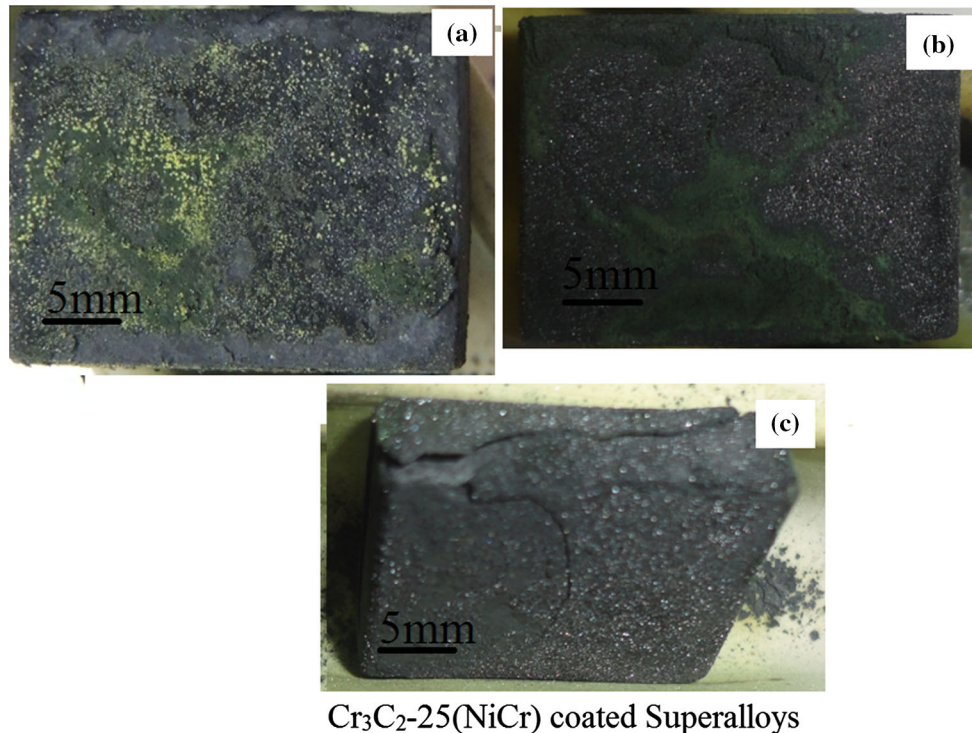


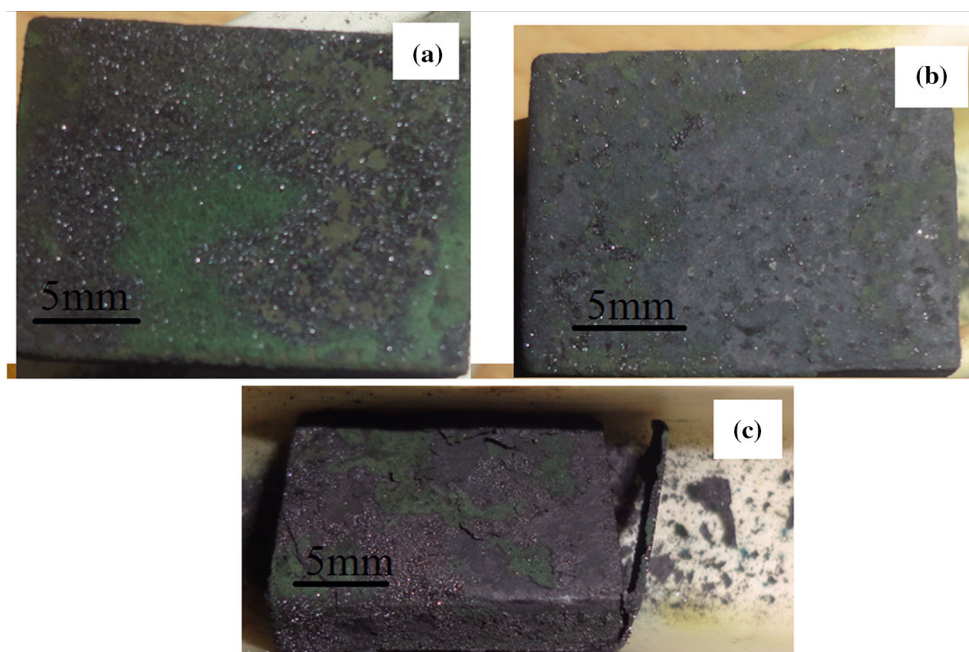
**Fig. 4** XRD analysis of  $\text{CeO}_2$ ,  $\text{Cr}_3\text{C}_2$ -NiCr and  $\text{Cr}_3\text{C}_2$ -NiCr + 0.4 wt.%  $\text{CeO}_2$  coating powders and as-sprayed coated Superni 718

vernier caliper (Swiss make, resolution 0.01 mm) to calculate the surface area. For hot-corrosion studies in the 40 %  $\text{Na}_2\text{SO}_4$  + 40 %  $\text{K}_2\text{SO}_4$  + 10 %  $\text{NaCl}$  + 10 %  $\text{KCl}$  environment, the samples were preheated in an oven at temperature of 250 °C before application of salt solution. The salt solution was made using distilled water in a china dish and applied to all six surfaces of the heated sample with the help of a camel-hair brush. Salt mixture was applied onto the samples at 3–5  $\text{mg}/\text{cm}^2$  only once before starting the cyclic hot-corrosion run. The amount of salt used for coating was selected based on previous reported literature (Ref 22, 25). The salt concentration in this study was chosen only to examine the hot-corrosion mechanism of the coating rather than for the actual conditions of coatings during operation (Ref 30). After salt application, the samples were placed in an oven at temperature of 110 °C for 2 h to evaporate the moisture content. All these prepared samples were subsequently subjected to cyclic hot-corrosion testing for 100 cycles at 900 °C in a silicon carbide tube furnace having a proportional–integral–derivative (PID) controller calibrated for accuracy of  $\pm 1$  °C. Each cycle consisted of 1 h of heating at 900 °C followed by 20 min of cooling in ambient air. During the experiment, each sample was kept in an alumina boat, and the weight of the boat along with the specimen was measured. This was taken as the initial sample weight at the start of the experiment. Weight change was noted down after each corrosion cycle. Each experiment was done twice, or sometime thrice, to cross-check results. The coated samples used in this study were classified as shown in Table 3.



$\text{Cr}_3\text{C}_2$ -25(NiCr) coated Superalloys

**Fig. 5** Macrophotos of  $\text{Cr}_3\text{C}_2$ -NiCr-coated (a) Superni 718, (b) Superni 600 and (c) Superalloy 605 after hot corrosion for 100 cycles under 40 %  $\text{Na}_2\text{SO}_4$ -40 %  $\text{K}_2\text{SO}_4$ -10 %  $\text{NaCl}$ -10 %  $\text{KCl}$  environment at 900 °C



$\text{Cr}_3\text{C}_2\text{-}25(\text{NiCr})+0.4\%\text{CeO}_2$  coated Superalloys

**Fig. 6** Macrophotos of  $\text{Cr}_3\text{C}_2\text{-NiCr} + 0.4 \text{ wt.}\% \text{CeO}_2$ -coated (a) Superni 718, (b) Superni 600 and (c) Superco 605 after hot corrosion for 100 cycles under 40 % $\text{Na}_2\text{SO}_4$ -40 % $\text{K}_2\text{SO}_4$ -10 % $\text{NaCl}$ -10 % $\text{KCl}$  environment at 900 °C

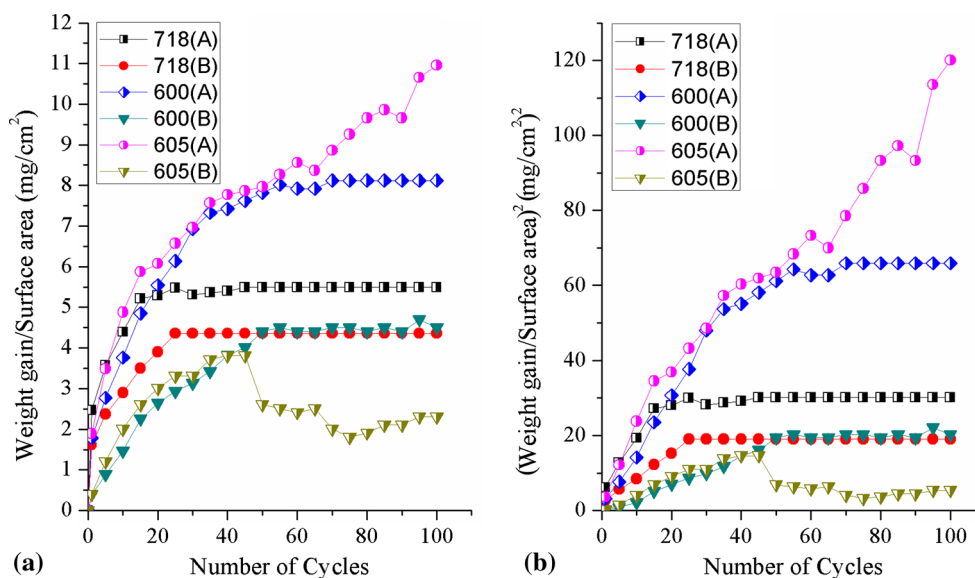


**Fig. 7** (a) Weight change/surface area and (b) (weight change/surface area)<sup>2</sup> versus number of cycles for coated specimens subjected to hot corrosion for 100 cycles at 900 °C

### 3. Results

#### 3.1 Microstructural Characterization of Coatings

Figure 2a and b show FESEM images of as-sprayed and polished top surface of  $\text{Cr}_3\text{C}_2\text{-NiCr}$  coating, respectively. The formation of a dense coating is seen in Fig. 2a. Semi-melted and partially melted particles were observed

on the surface of the as-sprayed coating. Mohanty et al. (Ref 31) reported that, in the D-gun process, powders to be deposited are fed into the combustion area by a carrier gas, where they are heated and carried by the gases exiting the nozzle. Molten or partially molten droplets arrive at the substrate, and flatten and solidify on impact. In Fig. 2b, the presence of chromium carbide particles was

observed in nickel chromium solid solution. Figure 2c clearly shows the presence of ceria particles along the splat boundaries in the case of ceria-doped  $\text{Cr}_3\text{C}_2\text{-NiCr}$  coating. Figure 3a and c show unpolished cross-sections of  $\text{Cr}_3\text{C}_2\text{-25(NiCr)}$ - and  $\text{Cr}_3\text{C}_2\text{-25(NiCr)+0.4 wt.\% CeO}_2$ -

coated alloys, respectively. Figure 3b and d show unpolished cross-sections of the specimens at higher magnification, clearly indicating the splats oriented parallel to the substrate. Figure 4 shows XRD patterns for as-received  $\text{CeO}_2$ ,  $\text{Cr}_3\text{C}_2\text{-NiCr}$  powder and  $\text{CeO}_2$ -doped  $\text{Cr}_3\text{C}_2\text{-NiCr}$  powders along with as-sprayed coating, depicting the presence of  $\text{Cr}_3\text{C}_2$  and Ni (solid solution of Cr in Ni) phase. The main difference observed between the XRD patterns of the coating powder and as-sprayed coating was an increase in the background intensity. This is due to the formation of an amorphous non-crystalline phase which appears in the thermal spray process because of the very fast cooling rate of the coating. Similar observation of peaks was reported by Magnani et al. (Ref 32). Microhardness measurements were taken at five different locations on the coating before and after the corrosion run,

**Table 4 Parabolic rate constants**

Parabolic rate constant ( $K_p$ ), $10^{-10} \text{ g}^2 \text{ cm}^{-4} \text{ s}^{-1}$	
Superalloy	Hot corrosion in molten salt at 900 °C
718(A)	3.0
718(B)	2.1
600(A)	9.3
600(B)	3.1

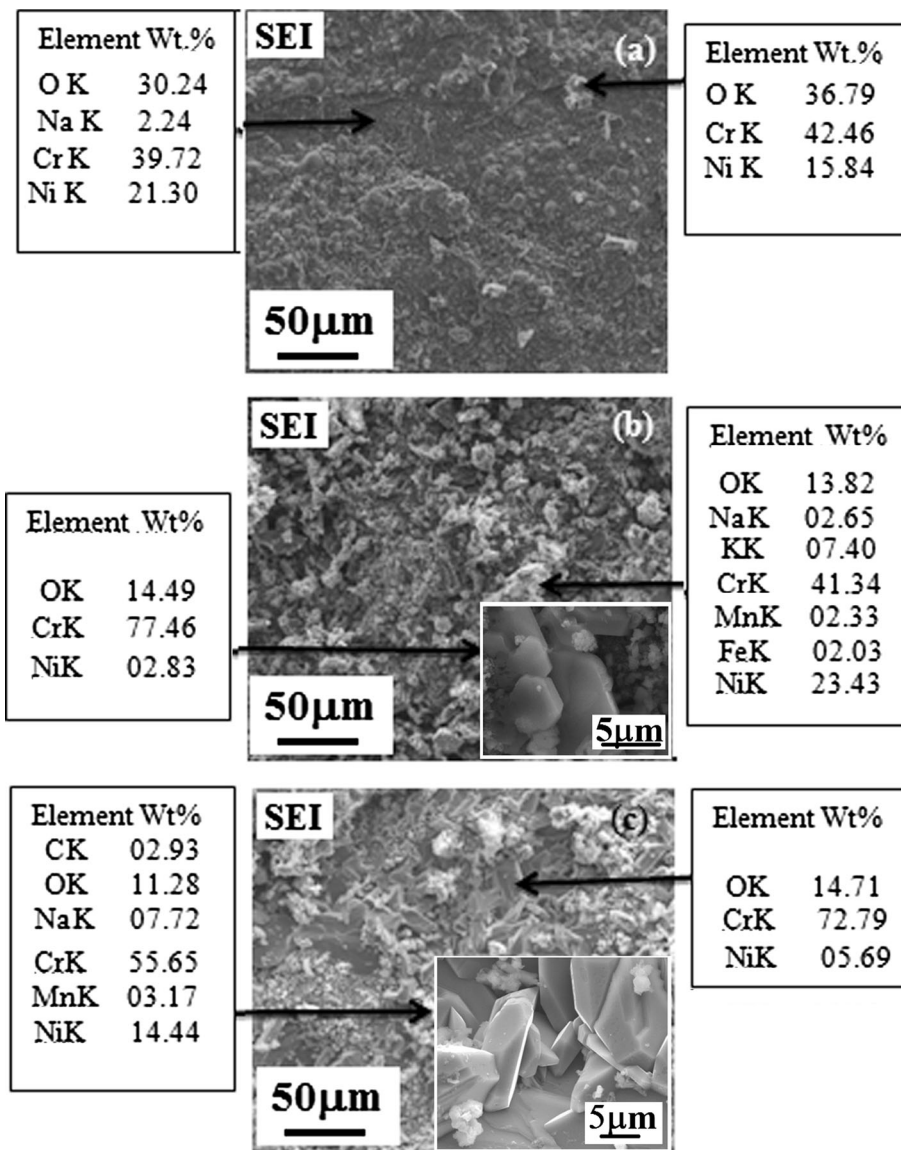


**Fig. 8** FESEM/EDS analysis of corroded  $\text{Cr}_3\text{C}_2\text{-NiCr}$ -coated (a) Superni 718, (b) Superni 600 and (c) Superco 605 after 100 cycles of hot corrosion under 40 % $\text{Na}_2\text{SO}_4$ -40 % $\text{K}_2\text{SO}_4$ -10 % $\text{NaCl}$ -10 % $\text{KCl}$  molten salt environment

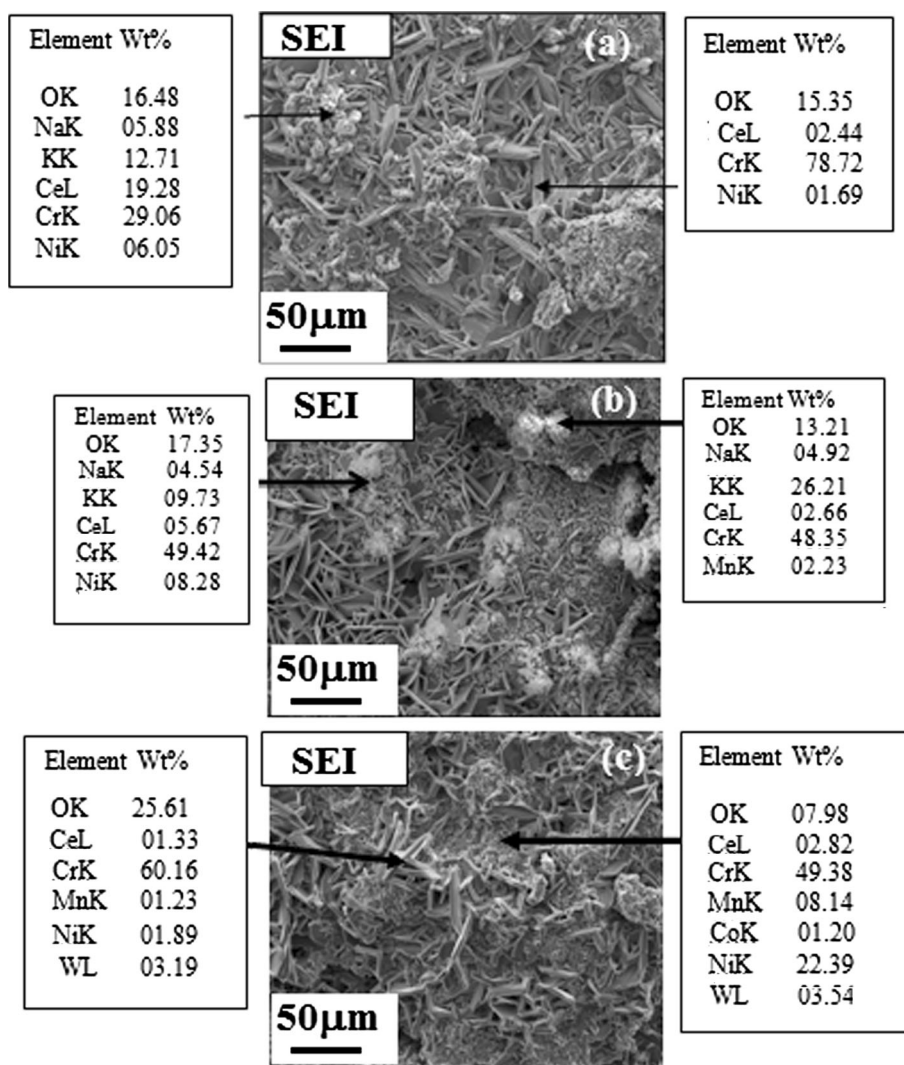


**Fig. 9** FESEM/EDS analysis of corroded  $\text{Cr}_3\text{C}_2\text{-NiCr} + 0.4\% \text{CeO}_2$ -coated (a) Superni 718, (b) Superni 600 and (c) Superco 605 after 100 cycles of hot corrosion under 40 % $\text{Na}_2\text{SO}_4$ -40 % $\text{K}_2\text{SO}_4$ -10 % $\text{NaCl}$ -10 % $\text{KCl}$  molten salt environment

being found to lie in the range from 650 to 950 Hv and 900 to 1300 Hv before and after the experiment, respectively, for coatings both with and without ceria doping. The average porosity, as measured by optical microscope, for coatings both with and without ceria doping was found to be 0.8 to 1%.

### 3.2 Visual Inspection

At the end of each hot-corrosion cycle, the boat with the sample was withdrawn from the furnace and cooled for 20 min in ambient air. The specimen was visually examined for any change in colour or any sign of spallation or sputtering. Macrophotos for the  $\text{Cr}_3\text{C}_2\text{-(NiCr)}$ - and  $\text{Cr}_3\text{C}_2\text{-(NiCr)} + 0.4 \text{ wt.}\% \text{CeO}_2$ -coated specimens after being subjected to hot corrosion for 100 cycles are shown in Fig. 5 and 6, respectively. In all cases, the colour of the coating changed from light grey to dark grey with dense greenish spots on the surface. In the case of 718(A),

yellowish-green oxide with dark-grey background appeared after just one cycle. Micro-spallation was also seen after the 5th cycle, continuing until the 37th cycle. After that, the micro-spallation ceased. Meanwhile, for the 718(B) sample, green oxide with dark-grey background was observed. In the case of 600(A), green-colour oxide appeared after 1 h of exposure and continued to intensify until the 50th cycle. A little micro-spallation was also noticed from the 7th cycle, continuing until the 17th cycle. However, in the case of ceria-doped coatings, no spallation was seen and the colour of oxide formed on the surface of the sample was dark grey with green patches. In the case of 605(A), dark-grey oxide was formed on the surface of coatings with green patches on it. It was also observed that a crack appeared on an edge after the 11th cycle. At the 14th cycle, the crack grew wider and the coating started to delaminate from all sides. At the 50th cycle, the coating was peeled off completely from all sides. Intense spallation was observed from the exposed areas of



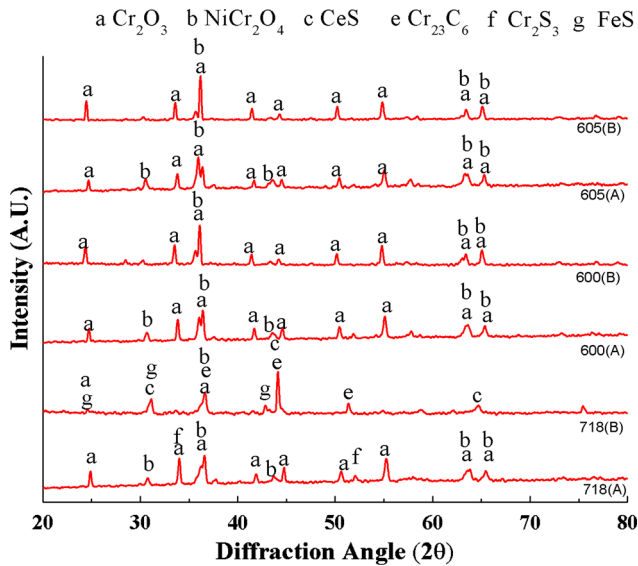


**Fig. 10** XRD analysis of corroded Cr<sub>3</sub>C<sub>2</sub>-NiCr- and Cr<sub>3</sub>C<sub>2</sub>-NiCr+0.4 wt.%CeO<sub>2</sub>-coated Superni 718, Superni 600 and Superco 605 after 100 cycles of hot corrosion under 40 %Na<sub>2</sub>SO<sub>4</sub>-40 %K<sub>2</sub>SO<sub>4</sub>-10 %NaCl-10 %KCl molten salt environment at 900 °C

Superco 605 starting from the 50th cycle until the 100th cycle. In the case of 605(B), delamination of the coating from one edge was observed, intensifying throughout the experiment after the 42nd cycle. Spallation in the form of powder was observed in the case of both 605(A) and 605(B) coatings under the given environment.

### 3.3 Weight Change Measurements

A graph of weight change per unit area against the number of cycles was plotted for all six coated substrates with and without ceria to determine the role of ceria during hot corrosion of these coatings in the given molten salt environment (Fig. 7a). Parabolic rate constants were calculated from graphs of the square of the weight change per unit area against the number of cycles (Fig. 7b) for 718(A), 718(B), 600(A) and 600(B) specimens and are presented in Table 4. The 605(A) sample showed parabolic behaviour until 35 cycles. After that, the specimen demonstrated an abrupt increase in weight until the 100th cycle. Meanwhile, the ceria-added coating sprayed on 605(B) followed parabolic behaviour until the 45th cycle, after which there was a loss in weight. The 600(A), 718(A), 600(B) and 718(B) samples exhibited parabolic behaviour. Ceria-doped Cr<sub>3</sub>C<sub>2</sub>-NiCr coating sprayed on all the substrates showed superior resistance to hot corrosion.

### 3.4 Surface Morphology

The surface morphology of the scale along with the EDS spectrum for the corroded coated superalloys after the cyclic hot corrosion at 900 °C are shown in Fig. 8 and 9. In the case of 718(A) (Fig. 8a), massive oxide was formed on the surface of the coating after 100 h of

exposure in the molten salt cyclic condition. From the EDS spectrum, the presence of Cr, Ni and O can be clearly noticed. Meanwhile, in the case of 718(B) (Fig. 9a), which is a ceria-doped coating, dense oxide with needle-like morphology can be seen, mainly consisting of Cr and O according to the EDS spectrum. Some dense patches were also seen throughout the surface of the coating, whose elemental analysis showed the presence of ceria in substantial quantity. In the case of Superni 600(A) (Fig. 8b), massive oxide with needle/platelet-like morphology was seen, consisting of Cr and O in major amounts along with some Ni, Na, K and S. Meanwhile, in the micrograph of 600(B) (Fig. 9b), the coating shows the formation of dense and compact oxide formed on the surface. Needle-like morphology was observed, along with some nodular structures. The EDS spectrum of the ceria-added coating 600(B) clearly shows the presence of a significant amount of ceria wherever dense patches exist on the surface of the coating. In the case of Superco 605(A) (Fig. 8c), massive oxide was observed, consisting of Cr and O as major elements. Meanwhile, for the Superco 605(B) sample (Fig. 9c), the oxide formed was dense with needle-like morphology, consisting of Cr and O along with ceria.

### 3.5 Phase Identification

X-ray diffractograms indicating the phases formed on the surface of corroded specimens are shown in Fig. 10. Formation of Cr<sub>2</sub>O<sub>3</sub> and NiCr<sub>2</sub>O<sub>4</sub> was noticed for 718(A), 718(B), 600(A), 600(B), 605(A) and 605(B). In the case of 718(A), the presence of minor peaks of Cr<sub>2</sub>S<sub>3</sub> was also observed. Meanwhile, in the case of ceria-containing coating sprayed onto Superni 718, major peaks of Cr<sub>23</sub>C<sub>6</sub>, CeS and FeS were also observed.

### 3.6 Cross-Sectional Analysis

Cross-sectional x-ray mapping of the samples after corrosion was carried out to describe the elemental distribution in the coating and scale. In the case of Superni 718(A), dense oxide scale mainly consisting of chromium and oxygen is indicated in Fig. 11. In the case of Superni 600(A) (Fig. 13), sodium can be seen, along with chromium and oxygen. In addition, diffusion of iron from the substrate towards the coating was also noticed. Figure 15 shows the elemental analysis of Superco 605(A), clearly indicating the presence of chromium along with oxygen throughout the scale. Cobalt and tungsten also diffused from the substrate into the coating. Presence of cobalt was seen inside the subscale region of the oxide scale. It was noticed that, at some sites where cobalt was present, chromium was absent. In the case of ceria-added coating sprayed onto Superni 718 (Fig. 12), the presence of thin and dense oxide of chromium and oxygen was observed. In the case of Superni 600(B) (Fig. 14), again the presence of chromium and oxygen was observed throughout the oxide. Manganese also diffused from the substrate into the coating. In the case of Superco 605(B) (Fig. 16), dense oxide consisting of chromium and oxygen

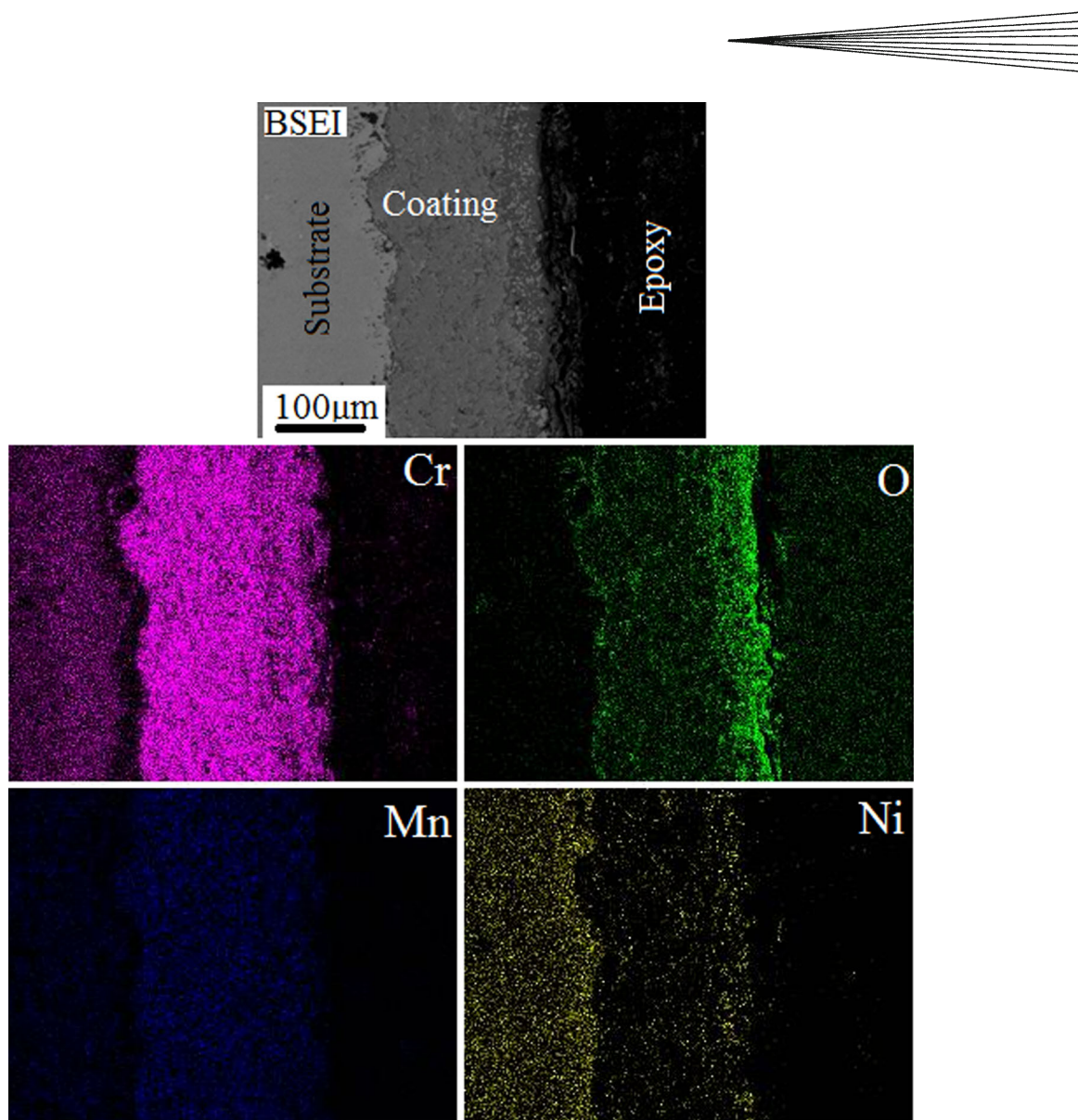


**Fig. 11** X-ray mapping of corroded  $\text{Cr}_3\text{C}_2$ -NiCr-coated Superni 718 after 100 cycles under 40 % $\text{Na}_2\text{SO}_4$ -40 % $\text{K}_2\text{SO}_4$ -10 % $\text{NaCl}$ -10 % $\text{KCl}$  molten salt environment

could be seen on the surface of the coating. Some unreacted metal was also observed in oxide scale. Presence of sulphur was also found in the subscale region of the oxide scale.

#### 4. Discussion

The SEM micrograph (Fig. 1c) of the ceria-doped coating powder indicates the presence of ceria particles embedded in a sponge-like matrix of  $\text{Cr}_3\text{C}_2$ -NiCr powder. In Fig. 2b, the light area represents NiCr metallic matrix, while the grey stringer corresponds to chrome carbide lamella. Similar observations have been made elsewhere (Ref 33, 34). In the coating, the carbide particles seem to appear well dispersed and well bonded within the structure. Pores appear black in the micrograph. The microstructure is characterized by a dense skeletal network of

fine chromium carbide bound within a ductile NiCr matrix. Similar features of as-sprayed D-gun-sprayed chrome carbide coating have been reported elsewhere (Ref 35). Cross-sectional images of unpolished  $\text{Cr}_3\text{C}_2$ -25(NiCr) coatings with and without ceria doping are shown in Fig. 3a and c. Plate-like lamellas oriented parallel to the substrate are clearly observed. Microhardness testing was performed before and after hot corrosion of 718(A) and 718(B), clearly depicting an increase in the microhardness of the uncorroded and corroded coating from the range of 725 to 905 Hv to the range of 1050 to 1230 Hv, respectively. Matthews et al. (Ref 19) also observed that high-temperature exposure of  $\text{Cr}_3\text{C}_2$ -NiCr coating led to transformations in the microstructure that influenced the coating microhardness. They suggested that the microhardness initially decreases, but with the course of time it increases due to precipitation and development of carbide phases.

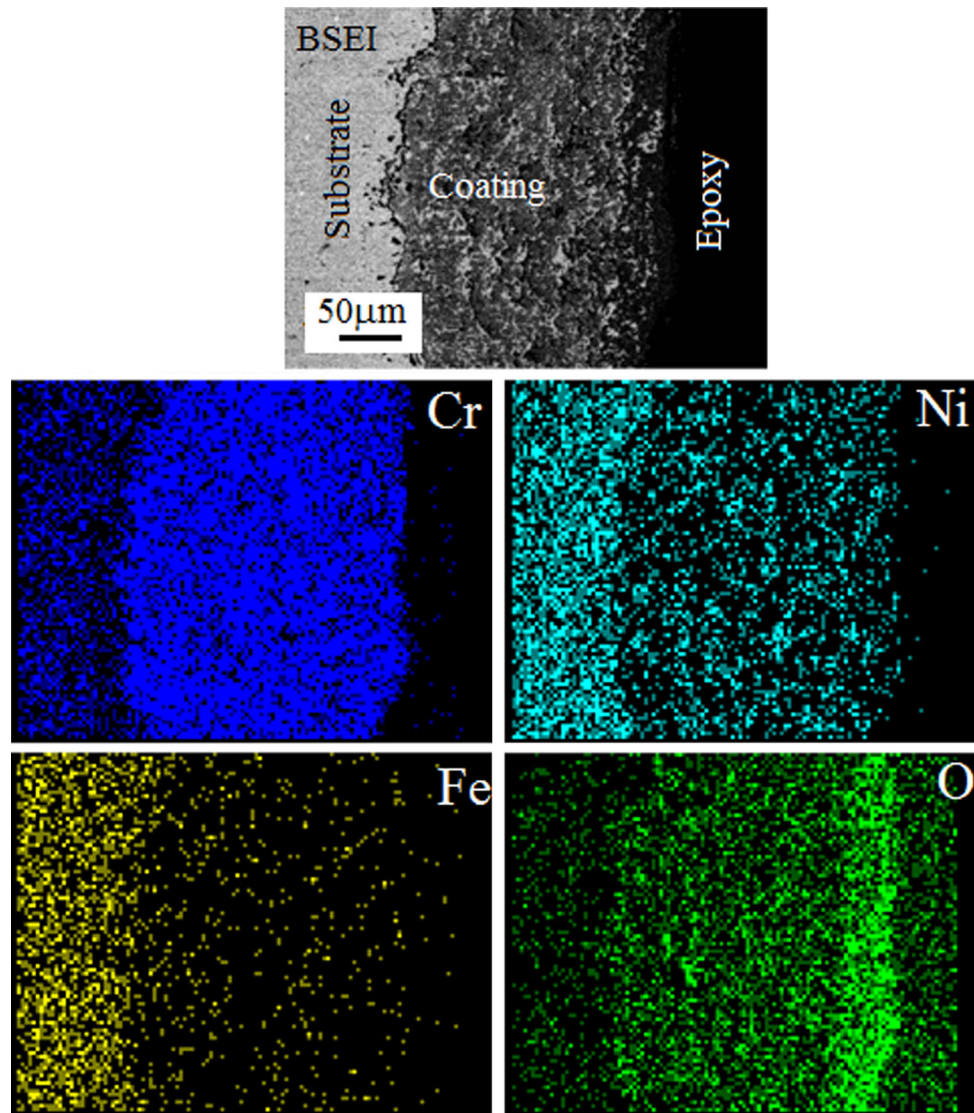


**Fig. 12** X-ray mapping of corroded  $\text{Cr}_3\text{C}_2\text{-NiCr} + 0.4\% \text{CeO}_2$ -coated Superni 718 after 100 cycles under 40 % $\text{Na}_2\text{SO}_4$ -40 % $\text{K}_2\text{SO}_4$ -10 % $\text{NaCl}$ -10 % $\text{KCl}$  molten salt environment

After the hot-corrosion run, the coated specimens 718(A) and 600(A) without ceria doping showed minor spallation during the initial cycles. Sidhu et al. (Ref 36) also reported the occurrence of minor sputtering in the case of  $\text{Cr}_3\text{C}_2\text{-NiCr}$  coating corroded under a  $\text{Na}_2\text{SO}_4$ -60 % $\text{V}_2\text{O}_5$  environment for 50 cycles at 900 °C. However, in the case of ceria-doped coatings, visual inspection indicated good adherence of the oxide scale on the coated specimens 718(B) and 600(B) up to 100 cycles of exposure. It was reported that rare-earth elements, as typified by yttrium, cerium and lanthanum, improve scale-substrate adhesion at high temperature. The scale so formed is more resistant to spalling or thermal cycling, hence reducing oxidation rates (Ref 37). Moon et al. (Ref 20) reported that oxide of reactive elements applied to a metallic substrate may improve the nucleation, growth and spallation characteristics of its oxide scale. Ecer et al. (Ref 38) also

suggested that the presence of surface-applied  $\text{CeO}_2$  improves scale adherence and results in marked changes in the oxidation morphology. Mikadze et al. (Ref 39) opined that small additions of Ce (0.5%) to Cr alloy had a fundamental influence on the formation of  $\text{Cr}_2\text{O}_3$  scale, redirecting the diffusion mass transfer from the dominant external diffusion of chromium to internal diffusion of oxygen. Kofstad (Ref 40) also suggested that rare-earth elements reduce the rate of oxide growth and improve oxidation resistance. This effect is presumably caused due to segregated oxides of rare-earth metals (REMs) at grain boundaries of  $\text{Cr}_2\text{O}_3$  scale, which is facilitated by internal diffusion of oxygen.

In this study, all the coated substrates showed initial higher weight gain. This may be due to rapid formation of oxides on the surface and at the coating splat boundaries, as well as due to penetration of oxidizing species along

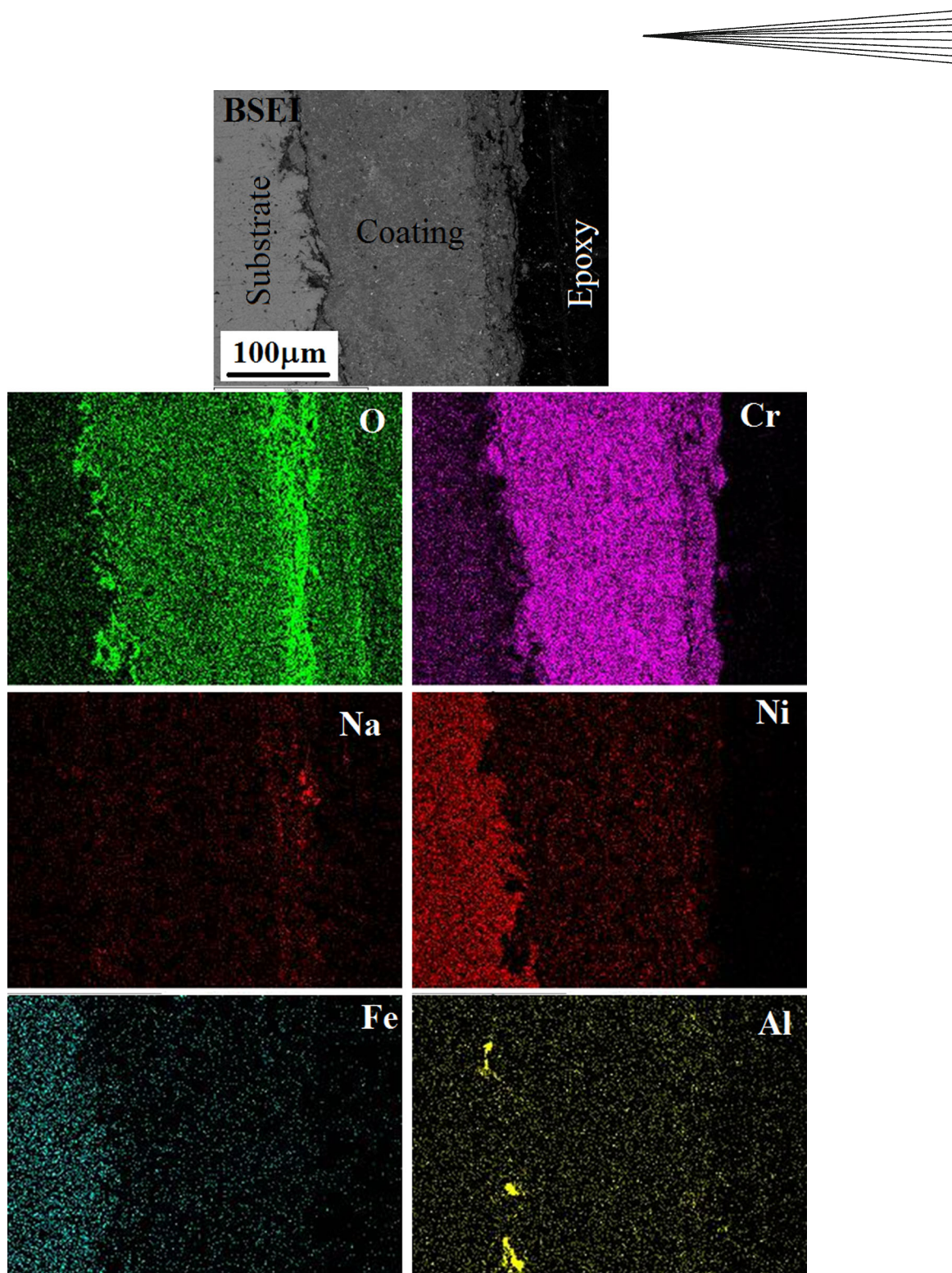


**Fig. 13** X-ray mapping of corroded  $\text{Cr}_3\text{C}_2$ -NiCr-coated Superni 600 after 100 cycles under 40 % $\text{Na}_2\text{SO}_4$ -40 % $\text{K}_2\text{SO}_4$ -10 %NaCl-10 %KCl molten salt environment

splat boundaries/open pores. Kamal et al. (Ref 41) also reported an initial higher weight gain in the case of D-gun-sprayed  $\text{Cr}_3\text{C}_2$ -(NiCr)-coated superalloys under a corrosive environment. Both coated Ni-based alloys (Superni 718 and Superni 600) showed good resistance under the given environment, as can be seen from the visual analysis

as well as the weight gain graphs. However, among these two, the coated Superni 718 showed better corrosion resistance, which may be due to the presence of aluminium in the substrate. In the case of Superco 605, coatings both with and without ceria doping started to delaminate from the surface of the alloy starting from the initial

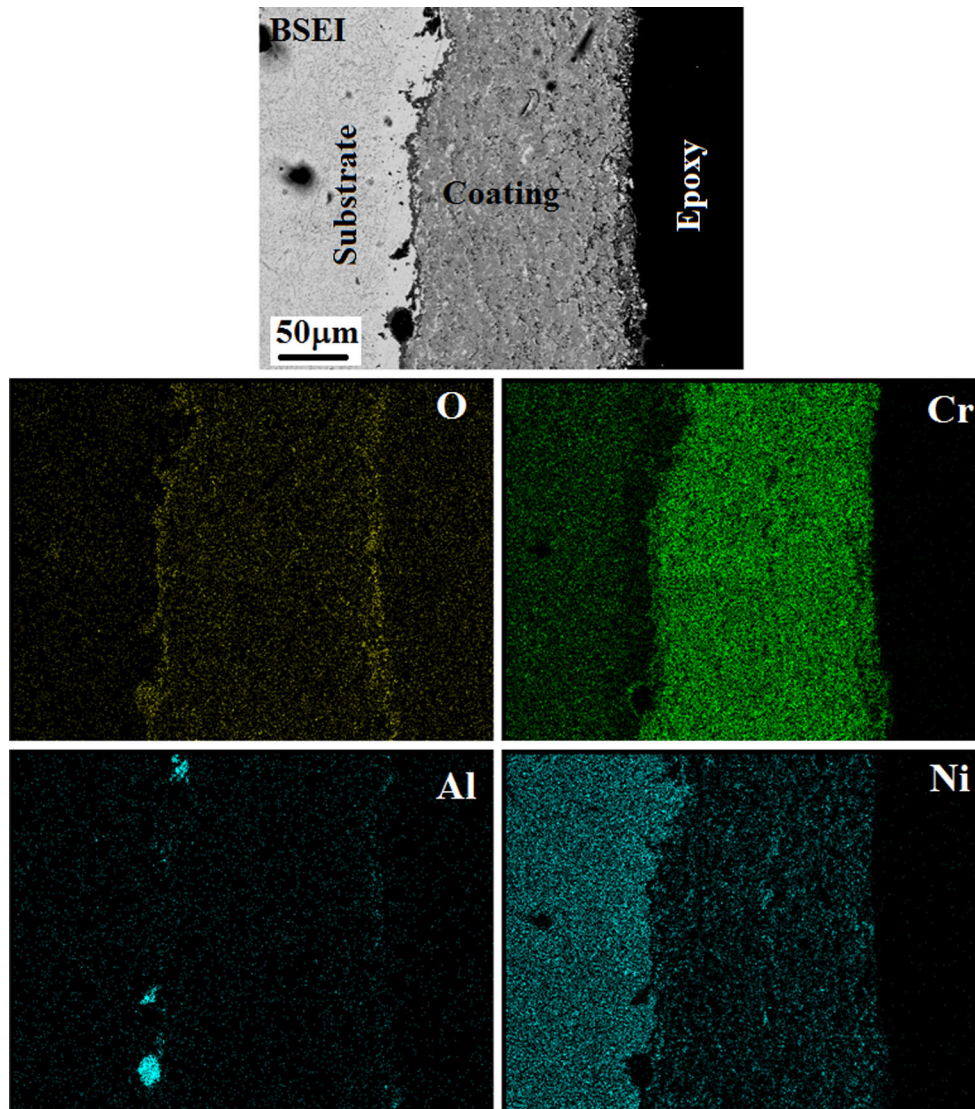


**Fig. 14** X-ray mapping of corroded  $\text{Cr}_3\text{C}_2\text{-NiCr}+0.4\% \text{CeO}_2$ -coated Superni 600 after 100 cycles under 40 % $\text{Na}_2\text{SO}_4$ -40 % $\text{K}_2\text{SO}_4$ -10 % $\text{NaCl}$ -10 % $\text{KCl}$  molten salt environment

cycles. Samples 605(A) and 605(B) corroded under the given environment deviated from the parabolic rate law and showed erratic behaviour. It was observed during experimentation that alloy 605(A) underwent abrupt increases in weight after a few cycles. This may be due to the delamination of the coating from the substrate. When the coating is completely detached, alloy 605(A) comes into direct contact with the corrosive environment. In previous literature (Ref 42), the corrosion behaviour of bare Supercor 605 under similar conditions was reported. It was observed that bare Supercor 605 showed severe weight gain in the given environment. Hence, in the present study also, when 605(A) exhibited direct contact with the environment after delamination, the alloy showed an abrupt increase in weight, which may be due to the huge spallation of exposed alloy.

In the case of 605(B), loss in weight was observed after a few cycles, followed by weight gain. The fluctuation of

weight was seen to be due to delamination of coating from one side only. As all other sides were still protected, the coated alloy did not show as much weight gain as in the case of 605(A). However, as one side of the alloy was now exposed to the environment, it reacted with the corrosive environment to form various oxides and chlorides. Here, the environment is chlorine based, and chlorine has a tendency to form volatile compounds (Ref 42). Hence, simultaneous formation of metal oxide and chlorine compounds ultimately led to the fluctuation in weight gain.

Macrophotos of corroded 605(A) after the 1st and 100th cycle are shown in Fig. 17. The extensive delamination observed from early hot-corrosion cycles may be due to formation of a Cr-W-rich layer in the substrate just below the coating-substrate interface, as can be seen from the x-ray mapping of the delaminated surface of 605(A) (Fig. 18). A similar result was reported by Warnes et al.

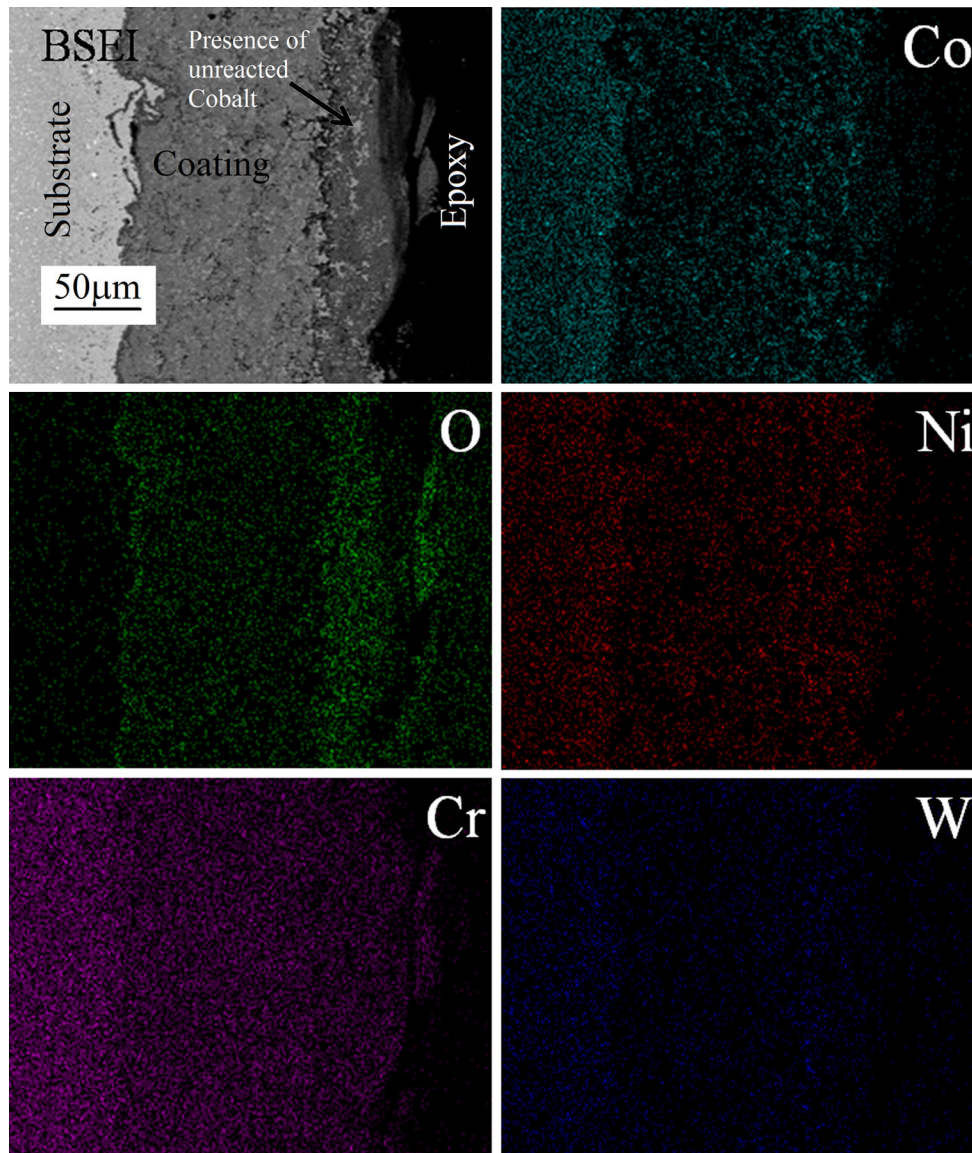
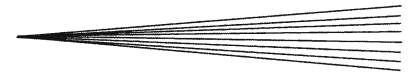


**Fig. 15** X-ray mapping of corroded  $\text{Cr}_3\text{C}_2\text{-NiCr}$ -coated Supercor 605 after 100 cycles under 40 % $\text{Na}_2\text{SO}_4$ -40 % $\text{K}_2\text{SO}_4$ -10 % $\text{NaCl}$ -10 % $\text{KCl}$  molten salt environment

(Ref 43) in a study of cyclic oxidation of diffusion aluminide coatings deposited on cobalt-base superalloys oxidized at 1,177 °C. They suggested that cracking of the Cr-W-rich layer formed at the coating-substrate interface alone could account for coating detachment. It may be contributed by the large difference in composition between the substrate and coating, which may result in a large difference between the thermal expansion coefficients of these materials. Lee et al. (Ref 44) also reported that mechanical failure is mainly due to stress build-up in the oxide and at the scale-metal interface that causes cracking and delamination of oxide scale. It is also reported in literature that the thermal spray process is not a good technique to deposit coatings on cobalt-base alloys. Instead, pack cementation has proved to be a more reliable method to coat these alloys, although it is a much

costlier method than thermal spray (Ref 45). The surface morphology of the oxide structure of coatings with and without ceria doping is shown in Fig. 8 and 9. In the case of the coating without added ceria, massive oxide can be seen throughout the surface along with needle/platelet-like morphology, supporting the formation of chromium oxide. EDS analysis also indicated the existence of chromium and oxygen at these sites. Sreedhar et al. (Ref 46) also reported that, in the case of NiCrAlY coating exposed under a  $\text{Na}_2\text{SO}_4$ -10 % $\text{NaCl}$  environment for 51 cycles, similar needle/platelet-type oxide structure was observed corresponding to that of chromium oxide, along with the presence of nickel-chromium-rich spinels. In the case of the ceria-doped coating, different morphology was observed in comparison with the coating without ceria doping after the hot-corrosion run. Some dense patches with

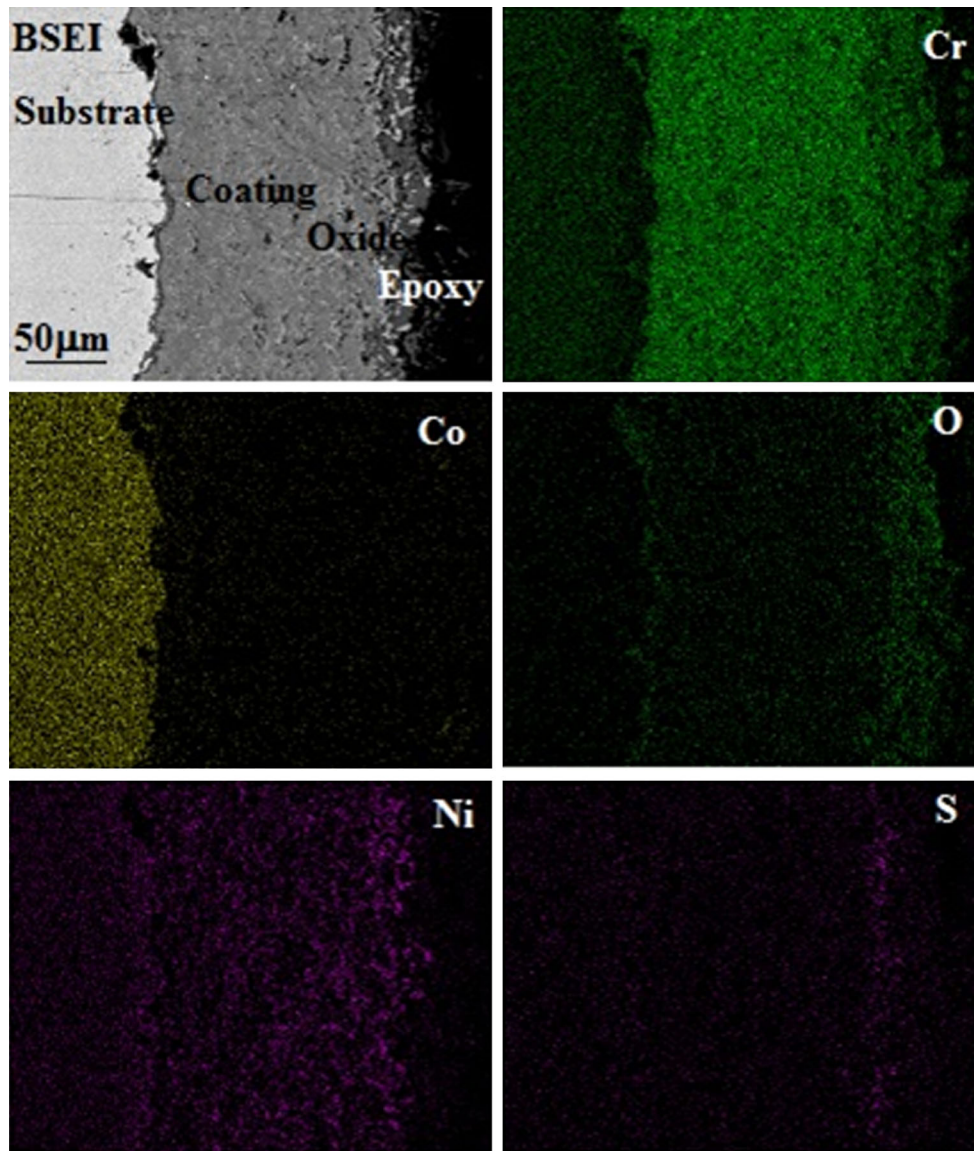


**Fig. 16** X-ray mapping of corroded  $\text{Cr}_3\text{C}_2\text{-NiCr}+0.4\% \text{CeO}_2$ -coated Supercor 605 after 100 cycles under 40 % $\text{Na}_2\text{SO}_4$ -40 % $\text{K}_2\text{SO}_4$ -10 % $\text{NaCl}$ -10 % $\text{KCl}$  molten salt environment

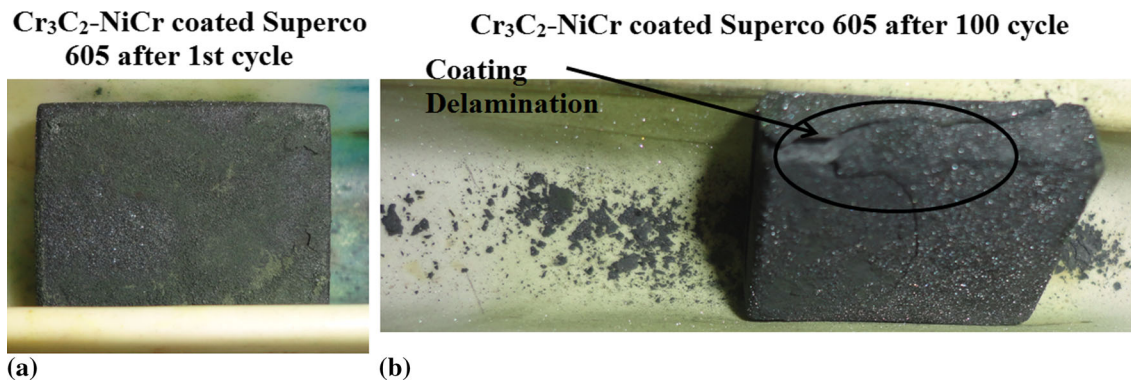


**Fig. 17** Macrophotos of corroded  $\text{Cr}_3\text{C}_2\text{-NiCr}$ -coated Supercor 605 after (a) 1st cycle and (b) 100th cycle under 40 % $\text{Na}_2\text{SO}_4$ -40 % $\text{K}_2\text{SO}_4$ -10 % $\text{NaCl}$ -10 % $\text{KCl}$  molten salt environment

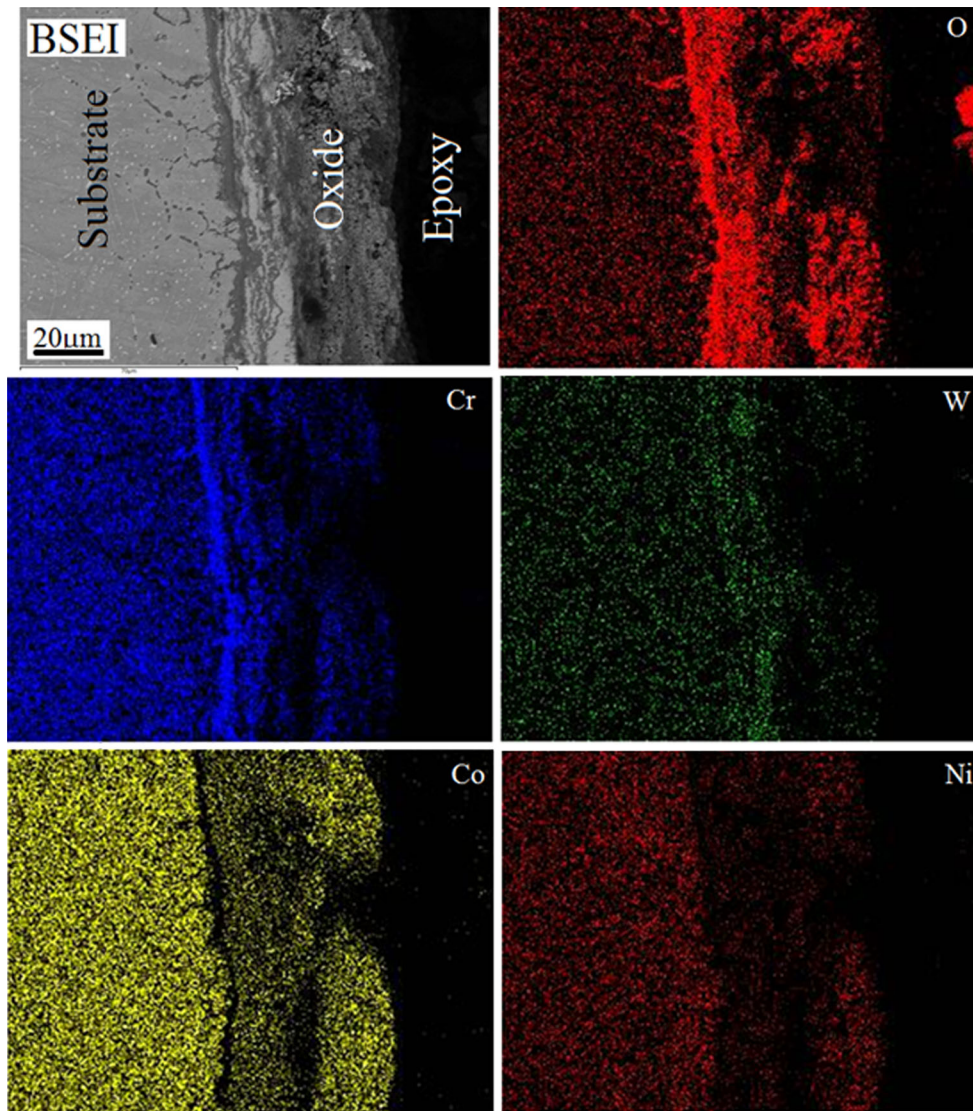
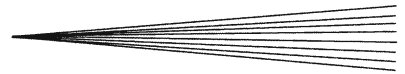
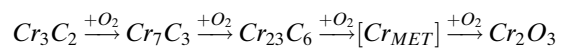


**Fig. 18** X-ray mapping of delaminated surface of corroded Cr<sub>3</sub>C<sub>2</sub>-NiCr-coated Superco 605 after 100 cycles under 40 %Na<sub>2</sub>SO<sub>4</sub>-40 %K<sub>2</sub>SO<sub>4</sub>-10 %NaCl-10 %KCl molten salt environment

cube-shaped clusters were observed in the case of both 718(B) and 600(B). EDS analysis taken at some sites clearly showed a higher amount of ceria at locations where dense patches were present, while presence of chromium and oxygen was seen in substantial amounts at the needle-like morphology. Fernandes et al. (Ref 47) suggested that specimens coated with rare-earth oxides formed cube, rod or needle-like morphology and platelet or cluster morphology depending on the RE used. They reported the existence of cube-like morphology in the case of surface application of ceria coating on Fe-20Cr alloy. Ramanathan (Ref 48) reported that, in the presence of Y or Ce, the oxide formed on the surface was convoluted and fine-grained chromia. It was also reported that the REMs are surface-active elements having a tendency to concentrate on the surface and help in forming a dense and uniform oxide layer. The oxide layer may act as a diffusion barrier,

thus delaying oxidation and corrosion processes (Ref 49, 50). XRD analysis of coated samples under the given environment showed the formation of Cr<sub>2</sub>O<sub>3</sub> and NiCr<sub>2</sub>O<sub>4</sub> in substantial amounts. Although the phase present in the coating before experimentation was Cr<sub>3</sub>C<sub>2</sub>, no peak of Cr<sub>3</sub>C<sub>2</sub> was recorded after hot-corrosion testing.

The formation of chromium oxide may be contributed by reaction of chromium present in the coating and oxidation of chromium carbide in a stepwise reaction leading to formation of Cr<sub>23</sub>C<sub>6</sub> or Cr<sub>2</sub>O<sub>3</sub> (Ref 51).



XRD analysis (Fig. 10) indicated the formation of Cr<sub>2</sub>O<sub>3</sub> and NiCr<sub>2</sub>O<sub>4</sub> in the case of all six corroded coated specimens. Formation of Cr<sub>2</sub>O<sub>3</sub> and NiCr<sub>2</sub>O<sub>4</sub> oxides was mainly responsible for the protection provided by the Cr<sub>3</sub>C<sub>2</sub>-NiCr



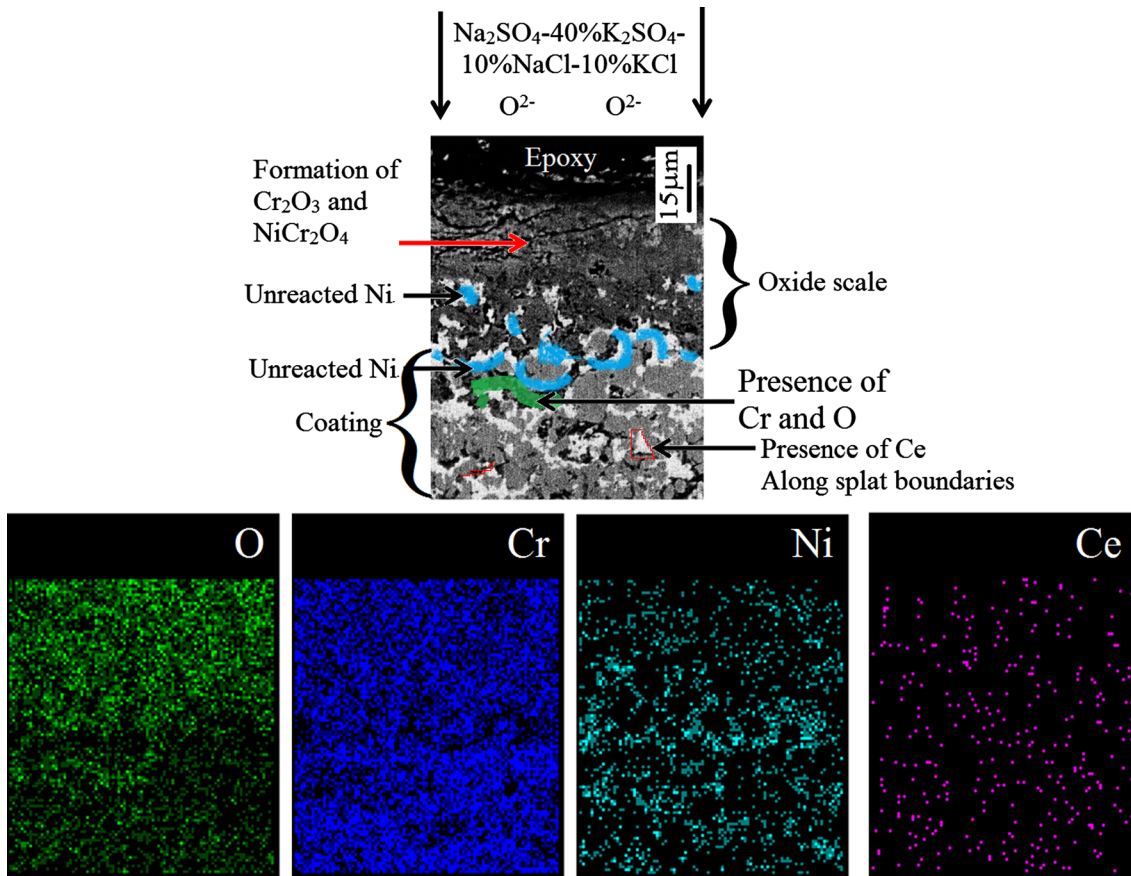
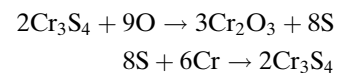


**Fig. 19** Probable schematic diagram of hot corrosion of  $\text{Cr}_3\text{C}_2\text{-NiCr} + 0.4 \text{ wt.}\% \text{CeO}_2$ -coated Superni 718 after 100 cycles under 40 % $\text{Na}_2\text{SO}_4$ -40 % $\text{K}_2\text{SO}_4$ -10 % $\text{NaCl}$ -10 % $\text{KCl}$  molten salt environment at 900 °C based on the cross-sectional elemental analysis given below

coating. It is well recognized that formation of  $\text{Cr}_2\text{O}_3$  is largely responsible for the superior oxidation resistance of nickel-based superalloys (Ref 52). It was also reported that the presence of  $\text{NiCr}_2\text{O}_4$  spinel in oxide scales also helps in developing oxidation resistance, as the spinel phases usually have much lower diffusion coefficients for cations and anions than in their parent oxides (Ref 53).  $\text{NiCr}_2\text{O}_4$  spinel was formed when  $\text{NiO}$  reacted with  $\text{Cr}_2\text{O}_3$  (Ref 54). New phases of  $\text{CeO}_2$  and  $\text{CeS}$  also appeared in the x-ray diffraction results in the case of ceria-doped coating. It was reported that cerium sulphide has a very high volatilization temperature of around 2450 °C and so is a stable phase up to 900 °C (Ref 55). Formation of  $\text{Cr}_{23}\text{C}_6$  was also indicated in Fig. 10 in the case of 718(B).

X-ray mapping was carried out to determine the chemical distribution. In x-ray mapping analysis, the presence of oxygen could be seen at splat boundaries in the case of all coatings. This is because of air entrapped within the splat boundaries during the coating deposition (Ref 56). Oxidation processes can occur during both the in-flight motion of the powder particles and exposure of the solidifying splats to the surrounding oxygen-rich atmosphere (Ref 57, 58). The higher oxide content of the coating could also affect its hardness, though the role of oxides is not well defined. Their higher hardness will

increase the overall hardness, while their presence as stringers may reduce splat/splat bonding, lowering the measured hardness (Ref 14). Presence of sulphur can also be observed in the subscale region of the oxide scale which formed on the top of the coating in Superco 605(B) (Fig. 16). Rizhang et al. (Ref 59) reported that, during hot corrosion of wrought Ni-16Cr-2Nb in the temperature range of 910–1020 °C, sulphur forms metallic sulphides by the following reactions:



Gurrappa (Ref 60) also supported the diffusion of sulphur into the substrate along grain boundaries and formation of metal sulphides in bare alloys. In Fig. 13 and 14, islands of aluminium along with oxygen are observed at the coating–substrate interface, although the islands do not match with the elements of either the coating or substrate. These islands are identified as aluminium oxides, possibly due to incorporation of alumina powder during polishing. Similar islands of aluminium oxides due to alumina powder retained during polishing were also reported by Sidhu et al. (Ref 61) and Sundararajan et al. (Ref 62). A schematic diagram showing the proposed hot-corrosion mechanism



for  $\text{Cr}_3\text{C}_2\text{-NiCr} + 0.4 \text{ wt. \% CeO}_2$ -coated Superni 718 superalloy after 100 cycles in  $\text{Na}_2\text{SO}_4 + 40 \text{ \% K}_2\text{SO}_4 + 10 \text{ \% NaCl} + 10 \text{ \% KCl}$  environment at  $900^\circ\text{C}$  is shown in Fig. 19. A corrosion mechanism for the case of  $\text{NiCrAlY} + 0.4 \text{ \% CeO}_2$ -coated Superfer 800 corroded under  $\text{Na}_2\text{SO}_4\text{-}60 \text{ \% V}_2\text{O}_5$  has been suggested by Kamal et al. (Ref 22). They reported that  $\text{CeO}_2$  was found to be distributed in the coating along splat boundaries.

## 5. Conclusions

1. Coated Superni 718 and Superni 600 showed a beneficial effect of ceria incorporation in the coating, reducing the weight gain by 20 and 44 %, respectively, during hot corrosion in  $\text{Na}_2\text{SO}_4 + 40 \text{ \% K}_2\text{SO}_4 + 10 \text{ \% NaCl} + 10 \text{ \% KCl}$  environment at  $900^\circ\text{C}$  for 100 cycles.
2. In the case of Superco 605,  $\text{Cr}_3\text{C}_2\text{-NiCr}$  with and without ceria did not perform very well in the hot-corrosion run, with a lot of delamination and spallation being observed from a very early stage of exposure.
3. SEM analysis of all the coatings clearly showed the variation in surface morphology of the coatings with and without ceria doping. In the case of coating without ceria doping, massive oxide along with needle-like morphology could be seen, while in ceria-doped coating some dense patches were observed throughout the surface, having clusters containing ceria in substantial amounts.
4. In the case of corroded coated Superni 718 and Superni 600,  $\text{Cr}_2\text{O}_3$  and  $\text{NiCr}_2\text{O}_3$  were the major oxides providing protection.

## References

1. J. Porcayo-Calderon, O. Sotelo-Mazon, V.M. Salinas-Bravo, C.D. Arrieta-Gonzalez, J.J. Ramos-Hernandez, and C. Cuevas-Arteaga, Electrochemical Performance of Ni20Cr Coatings Applied by Combustion Powder Spray in  $\text{ZnCl}_2\text{-KCl}$  Molten Salts, *Int. J. Electrochem. Sci.*, 2012, **7**, p 1134-1148
2. G. Sorell, The Role of Chlorine in High Temperature Corrosion in Waste-to-Energy Plants, *Mater. High Temp.*, 1997, **14**(3), p 137-150
3. T.S. Sidhu, R.D. Agrawal, and S. Prakash, Hot Corrosion of Some Superalloys and Role of High-Velocity Oxy-fuel Spray Coatings—A Review, *Surf. Coat. Technol.*, 2005, **198**(1-3), p 441-446
4. R. Venkataraman, B. Ravikumar, R. Krishnamurthy, and D.K. Das, A Study on Phase Stability Observed in as Sprayed Alumina-13 wt% Titania Coatings Grown by Detonation Gun and Plasma Spraying on Low Alloy Steel Substrates, *Surf. Coat. Technol.*, 2006, **201**, p 3087-3095
5. S. Kamal, R. Jayaganthan, and S. Prakash, Mechanical and Microstructural Characteristics of Detonation Gun Sprayed  $\text{NiCrAlY} + 0.4 \text{ wt \% CeO}_2$  Coatings on Superalloys, *Mater. Chem. Phys.*, 2010, **122**, p 262-268
6. S. Kamal, R. Jayaganthan, S. Prakash, and S. Kumar, Hot Corrosion Behavior of Detonation Gun Sprayed  $\text{Cr}_3\text{C}_2\text{-NiCr}$  Coatings on Ni and Fe-Based Superalloys in  $\text{Na}_2\text{SO}_4\text{-}60 \text{ \% V}_2\text{O}_5$  Environment at  $900^\circ\text{C}$ , *J. Alloys Compd.*, 2008, **463**, p 358-372
7. G.-C. Ji, C.-J. Li, Y.-Y. Wang, and W.-Y. Li, Erosion Performance of HVOF-Sprayed  $\text{Cr}_3\text{C}_2\text{-NiCr}$  Coatings, *J. Therm. Spray Technol.*, 2007, **16**(4), p 557-565
8. J. Wang, L. Zhang, B. Sun, and Y. Zhou, Study of the  $\text{Cr}_3\text{C}_2\text{-NiCr}$  Detonation Spray Coating, *Surf. Coat. Technol.*, 2000, **130**, p 69-73
9. M. Roy, A. Pauschitz, J. Wernisch, and F. Franek, The Influence of Temperature on the Wear of  $\text{Cr}_3\text{C}_2\text{-}25(\text{Ni}20\text{Cr})$  Coating—Comparison between Nanocrystalline Grains and Conventional Grains, *Wear*, 2004, **257**, p 799-811
10. H.S. Sidhu, B.S. Sidhu, and S. Prakash, Wear Characteristics of  $\text{Cr}_3\text{C}_2\text{-NiCr}$  and WC-Co Coatings Deposited by LPG Fueled HVOF, *Tribol. Int.*, 2010, **43**(5-6), p 887-890
11. J.K.N. Murthy and B. Venkataraman, Abrasive Wear Behaviour of WC-CoCr and  $\text{Cr}_3\text{C}_2\text{-}20(\text{NiCr})$  Deposited by HVOF and Detonation Spray Processes, *Surf. Coat. Technol.*, 2006, **200**(8), p 2642-2652
12. X.M. Li, Y.Y. Yang, T.M. Shao, Y.S. Jin, and G. Berbezat, Impact Wear Performances of  $\text{Cr}_3\text{C}_2\text{-NiCr}$  Coatings by Plasma and HVOF Spraying, *Wear*, 1997, **202**, p 208-214
13. Manpreet Kaur, Harpreet Singh, and Satya Prakash, Surface Engineering Analysis of Detonation-Gun Sprayed  $\text{Cr}_3\text{C}_2\text{-NiCr}$  Coating under High-Temperature Oxidation and Oxidation-Erosion Environments, *Surf. Coat. Technol.*, 2011, **206**, p 530-541
14. S. Matthews, B. James, and M. Hyland, The Role of Microstructure in the High Temperature Oxidation Mechanism of  $\text{Cr}_3\text{C}_2\text{-NiCr}$  Composite Coatings, *Corr. Sci.*, 2013, **70**, p 203-211
15. S.S. Chatha, H.S. Sidhu, and B.S. Sidhu, High Temperature Hot Corrosion Behaviour of NiCr and  $\text{Cr}_3\text{C}_2\text{-NiCr}$  Coatings on T91 Boiler Steel in an Aggressive Environment at  $750^\circ\text{C}$ , *Surf. Coat. Technol.*, 2012, **206**, p 4212-4224
16. S. Kumar, D. Mudgal, S. Singh, and S. Prakash, Cyclic Oxidation Behavior of Bare and  $\text{Cr}_3\text{C}_2\text{-}25(\text{NiCr})$  Coated Super Alloy at Elevated Temperature, *Adv. Mater. Lett.*, 2013, **4**(10), p 754-761
17. H.S. Sidhu, B.S. Sidhu, and S. Prakash, Cyclic Hot Corrosion of High-Velocity Oxy Fuel Sprayed Coatings on Steel at  $900^\circ\text{C}$ , *Corrosion*, 2006, **62**(11), p 1028-1038
18. T.S. Sidhu, S. Prakash, and R.D. Agrawal, Characterizations and Hot Corrosion Resistance of  $\text{Cr}_3\text{C}_2\text{-NiCr}$  Coating on Ni-Base Superalloys in an Aggressive Environment, *J. Therm. Spray Technol.*, 2006, **15**(4), p 811-816
19. S. Matthews, M. Hyland, and B. James, Microhardness Variation in Relation to Carbide Development in Heat Treated  $\text{Cr}_3\text{C}_2\text{-NiCr}$  Thermal Spray Coatings, *Acta Mater.*, 2003, **51**, p 4267-4277
20. D.P. Moon and M.J. Bennett, The Effects of Reactive Element Oxide Coatings on the Oxidation Behaviour of Metals and Alloys at High Temperatures, *Mater. Sci. Forum*, 1989, **43**, p 269-298
21. T. Amano, S. Yajima, and Y. Saito, High Temperature Oxidation of Ni-20Cr-5Al Alloys with Small Additions of Cerium, *T. Jpn. I. Met.*, 1985, **26**(6), p 433-443
22. S. Kamal, R. Jayaganthan, and S. Prakash, Hot Corrosion Studies of Detonation-Gun-Sprayed  $\text{NiCrAlY} + 0.4 \text{ wt \% CeO}_2$  Coated Superalloys in Molten Salt Environment, *J. Mater. Eng. Perform.*, 2010, **20**(6), p 1068-1077
23. R.A. Mahesh, R. Jayaganthan, and S. Prakash, A Study on the Oxidation Behavior of HVOF Sprayed  $\text{NiCrAlY-}0.4 \text{ wt \% CeO}_2$  Coatings on Superalloys at Elevated Temperature, *Mater. Chem. Phys.*, 2010, **119**(3), p 449-457
24. R.A. Mahesh, R. Jayaganthan, and S. Prakash, Characterisation of HVOF Sprayed  $\text{NiCrAlY-}0.4 \text{ wt \% CeO}_2$  Coatings on Superalloys, *Surf. Eng.*, 2008, **24**(5), p 366-373
25. R.A. Mahesh, G. Rao, R. Jayaganthan, and S. Prakash, Hot Corrosion Behaviour of HVOF Sprayed  $\text{NiCrAlY-}0.4 \text{ wt \% CeO}_2$  Coatings on Superalloys in Aggressive Environment at  $900^\circ\text{C}$ , *Corr. Sci. Technol.*, 2010, **45**(2), p 142-149
26. X. Song, L. Wang, Y. Liu, and H. MA, Effects of Temperature and Rare Earth Content on Oxidation Resistance of Ni-Based Superalloy, *Prog. Nat. Sci. Mater. Int.*, 2011, **21**, p 227-235
27. M.A. Uusitalo, P.M.J. Vuoristo, and T.A. Mäntylä, High Temperature Corrosion of Coatings and Boiler Steels below Chlorine-Containing Salt Deposits, *Corr. Sci.*, 2004, **46**, p 1311-1331

28. D.A. Shores and B.P. Mohanty, Role of Chlorides in Hot Corrosion of a Cast Fe-Cr-Ni Alloy. Part II: Thermochemical Model Studies, *Corr. Sci.*, 2004, **46**, p 2909-2924
29. T. Ishitsuko and K. Nose, Stability of Protective Oxide Films in Waste Incineration Environment—Solubility Measurement of Oxides in Molten Chlorides, *Corr. Sci.*, 2002, **44**(2), p 247-263
30. S. Yugeswaran, A. Kobayashi, and P.V. Ananthapadmanabhan, Hot Corrosion Behaviors of Gas Tunnel Type Plasma Sprayed  $\text{La}_2\text{Zr}_2\text{O}_7$  Thermal Barrier Coatings, *J. Eur. Ceram. Soc.*, 2012, **32**(4), p 823-834
31. M. Mohanty, R.W. Smith, M. De Bonte, L.P. Celis, and E. Lugscheider, Sliding Wear Behavior of Thermally Sprayed 75/25  $\text{Cr}_3\text{C}_2$ -NiCr Wear Resistant Coatings, *Wear*, 1996, **198**, p 251-266
32. M. Magnani, P.H. Suegama, N. Espallargas, C.S. Fugivara, S. Dosta, J.M. Guilemany, and A.V. Benedetti, Corrosion and Wear Studies of  $\text{Cr}_3\text{C}_2$ -NiCr-HVOF Coatings Sprayed on AA7050 T7 under Cooling, *J. Therm. Spray Technol.*, 2009, **18**(3), p 353-363
33. B. Yin, G. Liu, H. Zhou, J. Chen, and F. Yan, Sliding Wear Behavior of HVOF-Sprayed  $\text{Cr}_3\text{C}_2$ -NiCr/ $\text{CeO}_2$  Composite Coatings at Elevated Temperature up to 800°C, *Tribol. Lett.*, 2010, **37**, p 463-475
34. P. Hivart and J. Crampon, Interfacial Indentation Test and Adhesive Fracture Characteristics of Plasma Sprayed Cermet  $\text{Cr}_3\text{C}_2$ /Ni-Cr Coatings, *Mech. Mater.*, 2007, **39**, p 998-1005
35. J. Wang, L. Zhang, B. Sun, and Y. Zhou, Study of the  $\text{Cr}_3\text{C}_2$ -NiCr Detonation Spray Coating, *Surf. Coat. Technol.*, 2000, **130**, p 69-73
36. H.S. Sidhu, B.S. Sidhu, and S. Prakash, The Role of HVOF Coatings in Improving Hot Corrosion Resistance of ASTM-SA210 GrA1 Steel in the Presence of  $\text{Na}_2\text{SO}_4$ - $\text{V}_2\text{O}_5$  Salt Deposits, *Surf. Coat. Technol.*, 2006, **200**, p 5386-5394
37. P. Elliot, A Practical Guide to High Temperature Alloys, *Mater. Des.*, 1991, **2**(6), p 299-307
38. G.M. Ecer, R.B. Singh, and G.H. Meier, The Influence of Superficially Applied Oxide Powders on the High-Temperature Oxidation Behavior of  $\text{Cr}_2\text{O}_3$ -Forming Alloys, *Oxid. Met.*, 1982, **18**(1-2), p 55-87
39. O. Mikadze and A. Kandelaki, Influence of Cerium Additives on High-Temperature Corrosion of Chromium, *Bull. Georg. Natl. Acad. Sci.*, 2010, **4**(3), p 73-75
40. P. Kofstad, *High Temperature Corrosion*, Elsevier Applied Science, London, 1988, p 558
41. S. Kamal, R. Jayaganthan, S. Prakash, and S. Kumar, Hot Corrosion Behavior of Detonation Gun Sprayed  $\text{Cr}_3\text{C}_2$ -NiCr Coatings on Ni and Fe-Based Superalloys in  $\text{Na}_2\text{SO}_4$ -60%  $\text{V}_2\text{O}_5$  Environment at 900°C, *J. Alloys Compd.*, 2008, **463**(1-2), p 358-372
42. D. Mudgal, S. Singh, and S. Prakash, Hot Corrosion Behavior of Some Superalloys in a Simulated Incinerator Environment at 900 °C, *J. Mater. Eng. Perform.*, 2014, **23**(1), p 238-249
43. Bruce M. Warnes, Nick S. DuShane, and Jack E. Cockerill, Cyclic Oxidation of Diffusion Aluminide Coatings on Cobalt Base Super Alloys, *Surf. Coat. Technol.*, 2001, **148**, p 163-170
44. W.H. Lee and R.Y. Lin, Hot Corrosion Mechanism of Intermetallic Compound  $\text{Ni}_3\text{Al}$ , *Mater. Chem. Phys.*, 2002, **77**(1), p 86-96
45. J.A. Petrusba and F.P. Talboom, Superalloy Coatings for Components for Gas Turbine Engine Applications, *Preprint of Paper Presented at the 1966 National Metal Congress*, 1966
46. G. Sreedhar and V.S. Raja, Hot Corrosion of YSZ/ $\text{Al}_2\text{O}_3$  Dispersed NiCrAlY Plasma-Sprayed Coatings in  $\text{Na}_2\text{SO}_4$ -10 wt% NaCl Melt, *Corros. Sci.*, 2010, **52**, p 2592-2602
47. S.M.C. Fernandes and L.V. Ramanathan, Effect of Surface Deposited Rare Earth Oxide Gel Characteristics on Cyclic Oxidation Behaviour of Fe20-Cr Alloys, *Mater. Res.*, 2006, **9**(2), p 199-203
48. L.V. Ramanathan, Role of Rare-Earth Elements on High Temperature Oxidation Behavior of Fe-Cr, Ni-Cr and Ni-Cr-Al Alloys, *Corr. Sci.*, 1993, **35**(5-8), p 871-878
49. M.F. Pillis, E.G. de Araujo, and L.V. Ramanathan, Effect of Addition of Rare Earth Oxide Concentrates on Oxidation Resistance of AISI, 304L, *Mater. Sci. Forum*, 2006, **530-531**, p 99-104
50. M.F. Pillis, E.G. de Araújo, and L.V. Ramanathan, Effect of Addition of Rare Earth Oxide Concentrates on Oxidation Behavior of AISI, 304L Stainless Steel, *TMS Lett.*, 2004, **1**(3), p 57-58
51. S. Matthews, B. James, and M. Hyland, The Effect of Heat Treatment on the Oxidation Mechanism of Blended Powder  $\text{Cr}_3\text{C}_2$ -NiCr Coatings, *J. Therm. Spray Technol.*, 2010, **19**(1-2), p 119-127
52. A. Karabela, L.G. Zhao, J. Tong, N.J. Simms, J.R. Nicholls, and M.C. Hardy, Effects of Cyclic Stress and Temperature on Oxidation Damage of a Nickel-Based Superalloy, *Mater. Sci. Eng. A*, 2011, **528**, p 6194-6202
53. H. Singh, D. Puri, S. Prakash, and R. Maiti, Characterization of Oxide Scales to Evaluate High Temperature Oxidation Behavior of Ni-20Cr Coated Superalloys, *Mater. Sci. Eng. A*, 2007, **464**(1-2), p 110-116
54. W.Z. Li, Y. Yao, Q.M. Wang, Z.B. Bao, J. Gong, C. Sun, and X. Jiang, Improvement of Oxidation-Resistance of NiCrAlY Coatings by Application of CrN or CrON Interlayer, *J. Mater. Res.*, 2008, **23**(2), p 341-352
55. K. Gibbard, *A thesis on High temperature synthesis of cerium sulphides and kinetic modelling*, University of Florida, Gainesville, 2005
56. T.S. Sidhu, A. Malik, S. Prakash, and R.D. Agarwal, Thermal Spray 2007: Global Coating Solutions. B.R. Marple, M.M. Hyland, Y.C. Lau, R.S. Lima, G. Montavon, Ed., ASM International, Beijing, 2007, p. 538-542
57. V.V. Sobolev and J.M. Guilemany, Oxidation of Coatings in Thermal Spraying, *Mater. Lett.*, 1998, **37**, p 231-235
58. A.M. Ahmed, R.H. Rangel, V.V. Sobolev, and J.M. Guilemany, In-Flight Oxidation of Composite Powder Particles during Thermal Spraying, *Int. J. Heat Mass Transf.*, 2001, **44**, p 4667-4677
59. Z. Rizhang, G. Manjiou, and Z. Yu, A Study of the Mechanism of Internal Sulfidation-Internal Oxidation During Hot Corrosion of Ni-Base Alloys, *Oxid. Met.*, 1987, **27**(5/6), p 253-265
60. I. Gurrappa, Hot Corrosion Behavior of CM 247 LC Alloy in  $\text{Na}_2\text{SO}_4$  and NaCl Environments, *Oxid. Met.*, 1999, **51**(5/6), p 353-382
61. T.S. Sidhu, S. Prakash, and R.D. Agrawal, Hot Corrosion Studies of HVOF Sprayed  $\text{Cr}_3\text{C}_2$ -NiCr and Ni-20Cr Coatings on Nickel-Based Superalloy at 900°C, *Surf. Coat. Technol.*, 2006, **201**, p 792-800
62. T. Sundararajan, S. Kuroda, T. Itagaki, and F. Abe, Steam Oxidation Resistance of Ni-Cr Thermal Spray Coatings on 9Cr-1Mo Steel. Part 1: 80Ni-20Cr, *ISIJ Int.*, 2003, **43**(1), p 95-103